







## The Long-term Monitoring Results of *Insight-HXMT* in the First 4 Yr Galactic Plane Scanning Survey

CHEN WANG <sup>1,2</sup> JIN-YUAN LIAO <sup>3</sup> JU GUAN,<sup>3</sup> YUAN LIU,<sup>1</sup> CHENG-KUI LI <sup>3</sup> NA SAI <sup>4,5</sup> QI LUO,<sup>3</sup> JING JIN <sup>3</sup>  
YI NANG,<sup>3</sup> AND SHUANG-NAN ZHANG <sup>3,2,1</sup>

<sup>1</sup>Key Laboratory of Space Astronomy and Technology, National Astronomical Observatories, Chinese Academy of Sciences, Beijing 100101, People's Republic of China

<sup>2</sup>University of Chinese Academy of Sciences, Beijing 100049, People's Republic of China

<sup>3</sup>Key Laboratory of Particle Astrophysics, Institute of High Energy Physics, Chinese Academy of Sciences, 19B Yuquan Road, Beijing 100049, People's Republic of China

<sup>4</sup>Department of Astronomy, School of Physics and Technology, Wuhan University, Wuhan 430072, China

<sup>5</sup>WHU-NAOC Joint Center for Astronomy, Wuhan University, Wuhan 430072, China

### ABSTRACT

The first X-ray source catalog of *Insight-HXMT* Galactic Plane ( $|b| < 10^\circ$ ) Scanning Survey (GPSS) is presented based on the data accumulated from June 2017 to August 2021. The 4 yr limit sensitivities at main energy bands can reach  $8.2 \times 10^{-12} \text{ erg s}^{-1} \text{ cm}^2$  (2–6 keV),  $4.21 \times 10^{-11} \text{ erg s}^{-1} \text{ cm}^2$  (7–40 keV) and  $2.78 \times 10^{-11} \text{ erg s}^{-1} \text{ cm}^2$  (25–100 keV). More than 1300 sources have been monitored at a wide band (1–100 keV), of which 223 sources have a signal-to-noise ratio greater than 5. We combined the GPSS data of *Insight-HXMT* and MAXI and found it is feasible to obtain more complete long-term light curves from their scanning results. The flux variabilities at different energy bands of the 223 bright sources are analyzed based on the excess variances. It is found that the fluxes of X-ray binaries are more active than those of supernova remnants and isolated pulsars. Different types of binaries, e.g., low-mass X-ray binaries (LMXBs), high-mass X-ray binaries (HMXBs), neutron star binaries, and black hole binaries, also distinctively show different regularities. In addition, the relations between the hardness ratio (HR) and excess variances, and HR and source types are analyzed. It is obvious that the HRs of HMXBs tend to be harder than those of LMXBs and HMXBs tend to be more active than those of LMXBs.

**Keywords:** Catalogs – Surveys – X-rays: general

### 1. INTRODUCTION

There are various X-ray sources in the universe, such as stars, X-ray binaries, gamma-ray bursts, active galactic nuclei, galaxy clusters, etc. They exhibit not only spatial distribution characteristics from inside to outside the Galaxy but also morphological characteristics from point to diffuse sources of various scales. Observing and studying these sources in the X-ray band is of great significance for the development of astronomy. For example, understanding the formation and evolutionary history of stars, galaxies, and the

universe, as well as the accretion and radiation processes of compact objects, etc.

As the influence of the absorption effect of the Earth's atmosphere, astronomical observations in the X-ray band must be carried out in space observations. A variety of X-ray astronomical satellites have been launched for decades, and they have advanced astronomy by conducting large numbers of observations of sources in different energy bands from different regions to different depths of the sky. The first all-sky X-ray survey was performed by Uhuru, which was launched on Dec. 12th, 1970 (Giacconi et al. 1971). It found 339 X-ray sources at 2–6 keV band (Forman et al. 1978), and identified radiation resulted from accretion process of compact objects (Forman et al. 1973). The first Wolter-I type imaging telescope HEAO–2 was launched in 1978, which has a higher sensitivity than any previous telescopes (Giacconi et al. 1979). It demonstrated that X-ray emission could be produced in all types of sources, including stars (Vaiana

Corresponding author: Chen Wang  
cwang@bao.ac.cn

Corresponding author: Jin-Yuan Liao  
liaojinyuan@ihep.ac.cn

1990) and supernova remnants (SNRs, Seward 1982), and also took our study of X-ray astronomy from the Galaxy to nearby galaxies (van Speybroeck et al. 1979; Long et al. 1981). ROSAT is an all-sky survey imaging telescope in the soft X-ray band (0.1–2.4 keV), which has further increased the sensitivity with lower instrument noise and better background shielding technology (Truemper 1982). A total of 145,060 sources had been found during this survey (Voges et al. 1999), increasing the number of known sources by two orders of magnitude. MAXI was launched in 2009, which is an all-sky monitor onboard the International Space Station. It covers the energy band 2–30 keV with high survey efficiency of one all-sky scan per 92 minutes (Matsuoka et al. 2009; Hori et al. 2018). A large quantity of scientific data has been accumulated during its orbiting period, with monitoring of long-term variabilities of X-ray sources, and discovering over 30 new sources. There are also many other satellites, which have their own advantages and complement with each other. For example, the coded-mask telescope INTEGRAL/IBIS has been observing the sky in hard X-ray bands (above 20 keV) since 2002 (Krivonos et al. 2021), while Swift has the capability of rapid positioning to newly discovered GRBs and making multiwavelength observations (Burrows et al. 2005). The SRG/ART-XC observes the sky with subarcminute angular resolution and excellent sensitivity above 2 keV. It has detected 867 sources at 4–12 keV in its first-year all-sky survey and expects to discover a significant number of new X-ray objects (Pavlin-sky et al. 2022). These satellites have discovered new X-ray sources or published catalogs during their operation, which have contributed to the development of astronomy. Some large-area surveys (e.g., all-sky or Galactic Plane or serendipitous surveys with sky-coverage larger than 3000 deg<sup>2</sup>) are listed in Table 1.

The *Hard X-ray Modulation Telescope* (dubbed as *Insight-HXMT*) is an X-ray astronomy satellite covering a wide energy band (1–250 keV) with large Fields of Views (FOVs, Zhang et al. 2020). It was launched on June 15th, 2017, with three main scientific payloads: the High Energy X-ray Telescope (HE), the Medium Energy X-ray Telescope (ME), and the Low Energy X-ray Telescope (LE). Details of the three payloads are listed in Table 2. The three telescopes are composed of 18 NaI(Tl)/CsI(Na) crystal detector units (HE, Liu et al. 2020), 1728 pixels of Si-PIN detectors (ME, Cao et al. 2019), and Swept Charge Device (SCD) sensor arrays (LE, Chen et al. 2020), respectively. They are collimating telescopes, and each contains three detector groups with an intersecting orientation angle of 60°. The FOVs during scanning observations are 5°.7 × 1°.1 (HE), 4° × 1° (ME), and 1°.6 × 6° (LE), respectively. The FOVs of the three telescopes are shown in Figure 1.

*Insight-HXMT* provides us with scientific data to statistically study the timescales, duty cycles and spatial distribution of different types of sources, etc. *Insight-HXMT* has three types of observations: pointing observation of X-ray sources, monitoring GRBs, and Galactic Plane Scanning Survey (GPSS). It spends about one-third of observation time on scanning the Galactic plane to monitor known sources and find new X-ray transients. We adopt a small-sky-area scanning strategy in GPSS, which divides the entire Galactic plane (0° <  $l$  < 360°, -10° <  $b$  < 10°) into several small regions, and performs a line-by-line scanning of each region. The schematic diagram of a small-sky-area scanning is shown in Figure 2. The early phase strategy, before April 2019, was designed with a scanning speed of 0°.06 s<sup>-1</sup> and a interval of 0°.8. It divided the Galactic Plane into 22 small regions, each of which has a radius of 10°. For finer scanning, the current strategy has 50 small regions with a radius of 7°, a speed of 0°.06 s<sup>-1</sup> and a interval of 0°.4. Thanks to the design of large effective area and wide-band coverage, *Insight-HXMT* not only has a high scanning efficiency (14° × 14° coverage every 2.3 hours) but also can monitor the radiation intensity of X-ray sources from soft to hard X-ray energy bands at the same time. Meanwhile, the large amount of observation time ensures intensive monitoring of X-ray sources within its visible sky areas. In addition, with the background shielding technology, LE can reach 5 $\sigma$  sensitivity of  $\sim 5.7 \times 10^{-11}$  erg s<sup>-1</sup> cm<sup>-2</sup> (1–6 keV, 2.5 mCrab) for each scanning observation ( $\sim 2.3$  h). Up to August 2021, *Insight-HXMT* has conducted over 2000 scanning observations, covering the entire Galactic plane. Exposure maps for the three telescopes are shown in the left column of Figure 3. Sensitivity maps for three main energy-bands are shown in the right column, with the best sensitivities up to  $8.2 \times 10^{-12}$  erg s<sup>-1</sup> cm<sup>-2</sup> (2–6 keV, 0.61 mCrab),  $4.2 \times 10^{-11}$  erg s<sup>-1</sup> cm<sup>-2</sup> (7–40 keV, 2.35 mCrab), and  $2.8 \times 10^{-11}$  erg s<sup>-1</sup> cm<sup>-2</sup> (25–100 keV, 2.2 mCrab), which are listed in Table 4. Long-term light curves for 1345, 957, and 935 X-ray sources are given by LE, ME, and HE, respectively.

In this paper, we report the GPSS results of *Insight-HXMT*, using the 4 yr data from June 2017 to August 2021. The data reduction and light-curve fitting methods are described in Section 2. The GPSS results and error analyses are presented in Section 3. We combine the long-term light curves from *Insight-HXMT* monitored at 2–4 keV with those from MAXI in Section 4 and perform a series of statistical analysis on the bright sources in Section 5. The conclusion and summary are presented in Section 6.

**Table 1.** Information of some X-ray missions.

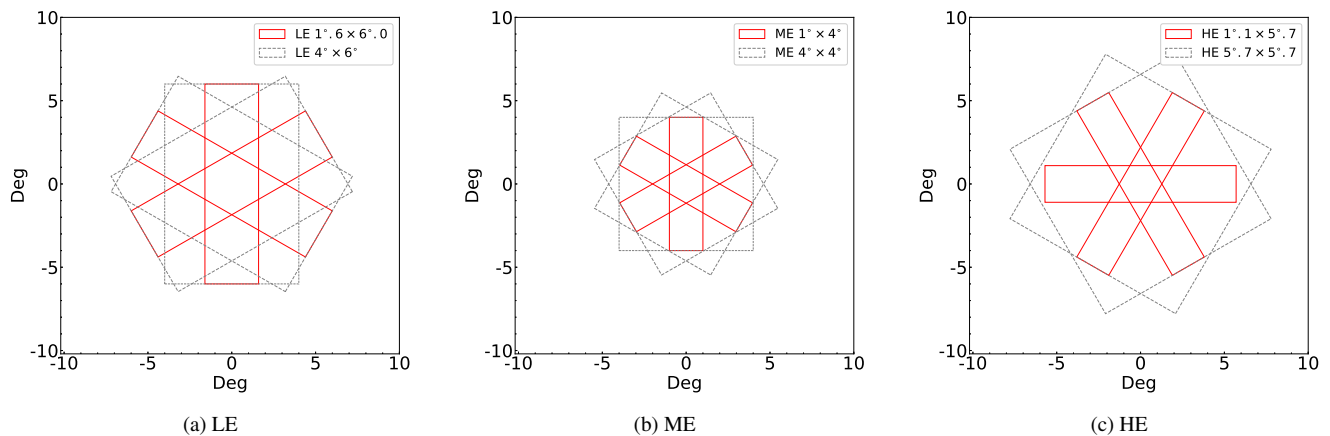
Mission <sup>a</sup>	Launch Date	Catalog	Energy Band (keV)	Scan Region	Sky Coverage (deg <sup>2</sup> )	Release Date	Reference
Uhuru	Dec. 12th, 1970	339	2 – 6	All – sky		1978	Forman et al. (1978)
Ariel V	Oct. 15th, 1974	109	2 – 10	$ b  < 10^\circ$		1981	Warwick et al. (1981)
HEAO – 1	Aug. 12th, 1977	842	0.5 – 25	All – sky		1983	Wood et al. (1984)
EXOSAT	May. 26th, 1983	1210	1 – 8	All – sky		1998	Reynolds et al. (1999)
ROSAT	Jun. 1th, 1990	135,000	0.1 – 2.4	All – sky		2016	Boller et al. (2016)
RXTE	Dec. 30th, 1995	294	3 – 20	serendipitous <sup>b</sup>	34,090	2004	Revnivtsev et al. (2004)
XMM – Newton	Dec. 10th, 1999	72,352	0.2 – 12	serendipitous	65,000	2017	XMMSL2 (2017)
<i>INTEGRAL</i>	Oct. 17th, 2002	929	17 – 60	All – sky		2021	Krivonos et al. (2021)
<i>Swift</i>	Nov. 20th, 2004	206,335	0.3 – 10	serendipitous	3,790	2020	Evans et al. (2020)
MAXI	Aug. 15th, 2009	221	4 – 10	$ b ^c < 10^\circ$		2018	Hori et al. (2018)
SRG/ART – XC	Jul. 19th, 2019	867	4 – 12	All – sky		2022	Pavlinisky et al. (2022)

NOTE—

<sup>a</sup> Here in the table we briefly list one of the catalogs for each mission, even though some missions have released several catalogs at various regions, different energy bands, or observation times. For example, HEAO-1 had provided catalogs at different energy bands, such as 842 sources at 0.5–25 keV (Wood et al. 1984), 114 sources at 0.18–0.44 keV (Nugent et al. 1983), 44 sources at 40–80 keV, and 14 sources at 80–180 keV (Levine et al. 1984).

<sup>b</sup> The survey is based on slew observations or a compilation of pointed observations.

<sup>c</sup> Outside the Galactic center region ( $|b| < 5^\circ$ ,  $l < 30^\circ$ , and  $l > 330^\circ$ ).

**Figure 1.** The FOVs of LE, ME and HE, respectively.

## 2. DATA REDUCTION AND LIGHT CURVE FITTING

### 2.1. Data Reduction

We have developed a set of pipelines to reduce the GPSS data. The general flowchart is shown in Figure 4. Step 1 is the extraction process of light curves from the raw data with *Insight-HMXT* data analysis software HXMTDAS v2.0 (HSDC 2020). In the next step, we estimate the background and further select Good Time Interval (GTI). GTI is generally related to the orbital environment of the satellite and can

be selected by the data analysis software. However, sometimes the LE data require extra selection, because the data at 1–6 keV band are vulnerable to contamination of particle events. The details are described in Sai et al. (2020). The backgrounds of HE and ME are characterized by the fluctuations that come from the modulation of geomagnetic field (Li et al. 2009; Xie et al. 2015), and a polynomial fit is sufficient enough to estimate them (Nang et al. 2020). The background of LE is generally weak and of low count rates dur-

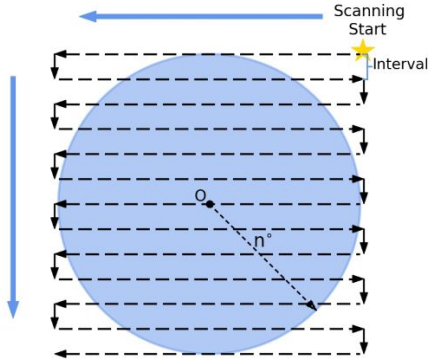


**Figure 2.** Schematic diagram of the scanning method of a small sky area. The circle is the observed area, and ‘O’ is the center of the circle. The arrow points to the scanning direction.

**Table 2.** Payloads of *Insight-HXMT*.

	HE	ME	LE
Geometrical Area (cm <sup>2</sup> )	5100	952	384
Small FOV (FWHM)	1° .1 × 5° .7	1° × 4°	1° .6 × 6°
Large FOV (FWHM)	5° .7 × 5° .7	4° × 4°	4° × 6°
Energy Band1 <sup>a</sup> (keV)	20 – 250	5 – 40	0.7 – 13
Energy Band2 <sup>b</sup> (keV)	25 – 100	7 – 40	1 – 7 <sup>c</sup>

NOTE—

<sup>a</sup> The energy bands that three instruments covered.

<sup>b</sup> The energy bands that used in *Insight-HXMT* GPSS.

<sup>c</sup> This energy band is sub-divided into 1–2 keV, 2–6 keV, 2–4 keV, 4–6 keV, 3–5 keV, 5–7 keV and 1–6 keV.

ing GTI. However, it often rises to a dramatically high level when particle events accumulate on the detectors or *Insight-HXMT* passes through the South Atlantic Anomaly (SAA) region (Liao et al. 2020). Consequently, it can be reliably estimated by the Statistics-sensitive Nonlinear Iterative Peak (SNIP) method (Morháč et al. 1997; Ryan et al. 1988).

To obtain high-quality scientific data to the maximum extent, the mean GTI coverage rates in each scan area of HE, ME, and LE are chosen to be 39.1 %, 31.5 %, and 27.7 %, respectively. Each telescope has covered the entire Galactic plane after completion of the first-year observation. They are all collimating telescopes and hence only the X-ray sources that cross the FOVs can be recorded. That the detection efficiency increases with decreasing orientation angle of the collimator induces a triangular peak on the light curve as the FOVs sweep through a source. The peak will change when the telescope sweeps different areas on account of the various brightness of X-ray sources. This can be analogized as

Point-Spread Function (PSF). The source position and flux can be reconstructed by fitting the corresponding light curves via PSF models. During the PSF fitting, the flux is assumed as a constant and hence the time-averaged value is obtained for each observation. It is accurate in most cases because an exposure for one target generally lasts within a few hundred seconds per observation, during which the flux variabilities of most sources are insignificant. The details of PSF fitting are given in Nang et al. (2020). To improve the positioning accuracy, we generate light curves according to the three collimator orientations in HE, ME, and LE, respectively.

## 2.2. Light Curve Fitting

To ensure the completeness of the X-ray sources in GPSS, the source catalog we adopted is a merge of catalogs from the websites of *Swift*<sup>1</sup>, *INTEGRAL*<sup>2</sup> and MAXI<sup>3</sup>. It contains 2881 sources in total, whereas some sources are located too close to be distinguished because of the limited angular resolution of *Insight-HXMT*. To improve the fitting efficiency, the sources that locate within 0° .6, 0° .6, and 0° .1 in HE, ME, and LE, are merged in our catalog, respectively. After the scanning data are screened, we fit the corresponding light curves with steps 3–7 illustrated in Figure 4. The details are described in Sai et al. (2020), and we outline the processes as follows:

1. Extract the known sources covered by the scan area from our catalog and find which of them are crossed by the FOVs via calculating their effective areas.
2. Fix the positions of the sources obtained in the previous step one after another and use the corresponding PSF models to estimate their fluxes.
3. Distinguish bright and faint sources based on the fluxes and signal-to-noise ratios (S/N). The source with flux higher than the detection limit and  $S/N > 2$  is defined as a bright source. Otherwise, it is a faint source, and the S/N is defined as

$$S/N = \frac{F}{\sigma}, \quad (1)$$

where  $F$  is the best-fitted flux, and  $\sigma$  the statistical uncertainty. In other words, bright sources mainly contribute to signal peaks in the light curves, and faint ones have no obvious contribution.

4. Freeze all positions and then fit the fluxes of bright sources simultaneously. The fluxes with the optimal

<sup>1</sup> <https://swift.gsfc.nasa.gov/results/transients/>

<sup>2</sup> [http://isdc.unige.ch/integral/catalog/43/gnrl\\_refr\\_cat\\_0043.html](http://isdc.unige.ch/integral/catalog/43/gnrl_refr_cat_0043.html)

<sup>3</sup> <http://134.160.243.88/top/slist.html>



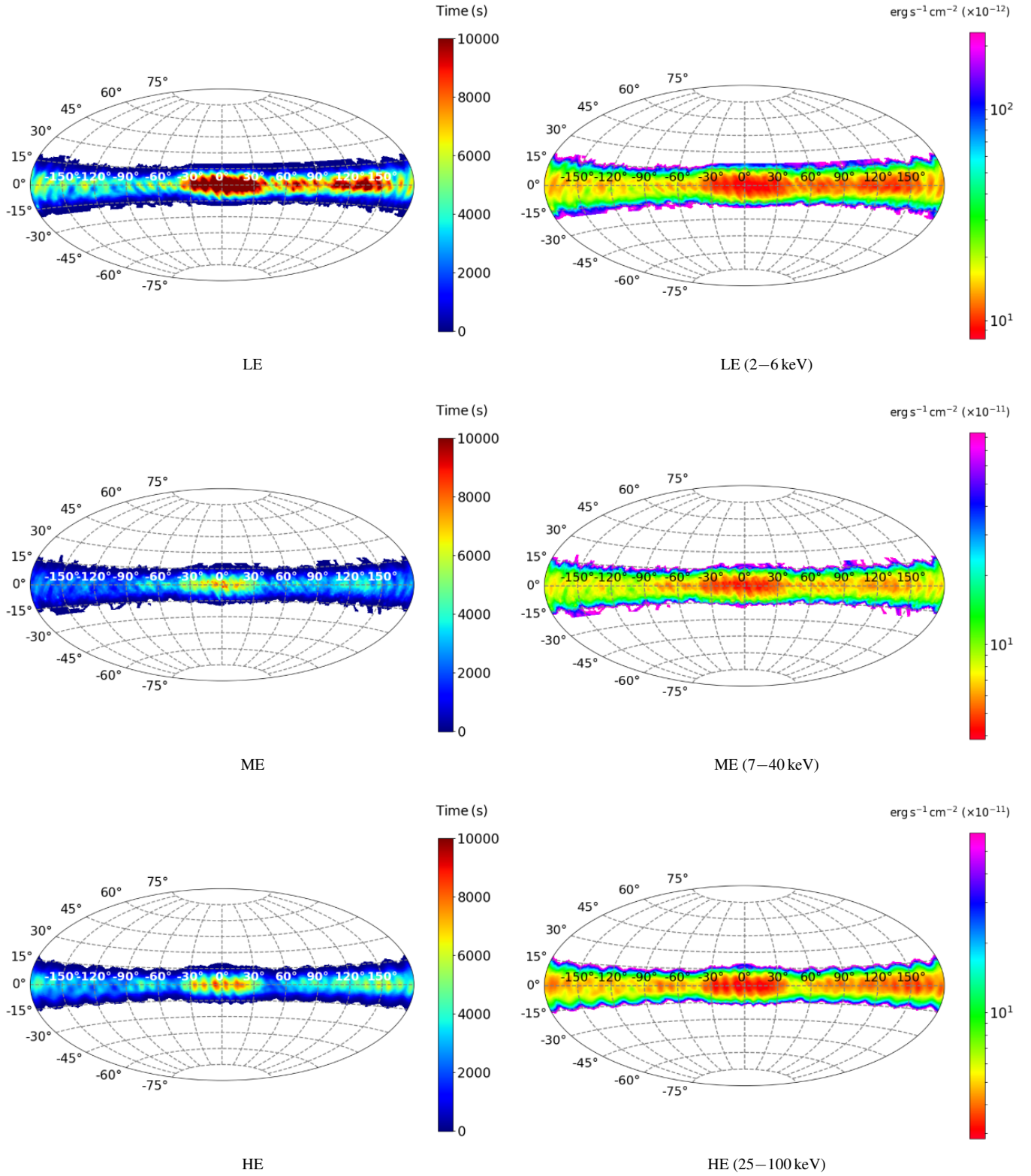


**Figure 3.** The exposure and sensitivity maps in the Galactic Plane for *Insight-HXMT* are shown in the left and right columns, respectively. In the left column, the colors correspond to the exposure time from 2017-06-29 to 2021-08-27. The difference in exposures between the three telescopes comes mainly from the difference in Good Time Intervals and FOV sizes. In addition, HE has less GPSS data than LE and ME because it spends some observation time on gamma-ray burst monitoring.

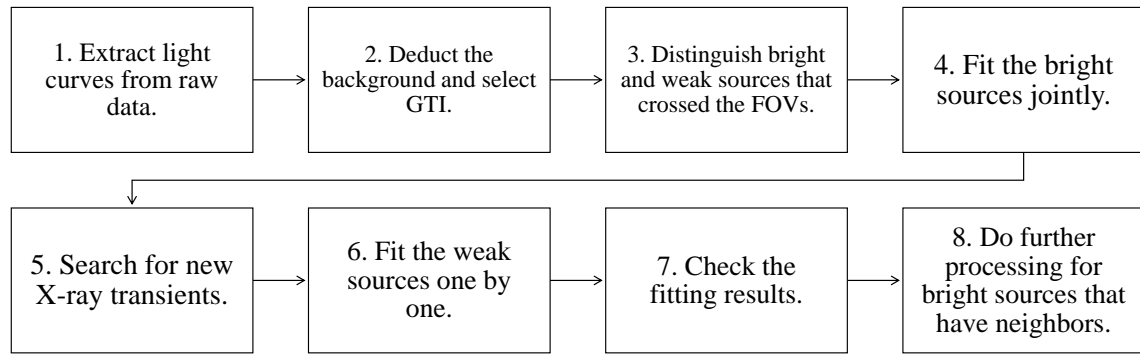


**Figure 4.** GPSS data analysis process.

chi-squared values are considered to be the final results. Hereafter, the jointly fitting method and the corresponding results are called as method 1 and results 1, respectively.

5. Search for the location and flux of a new source candidate based on the residuals of the previous step.
6. Fit the faint sources with a single PSF model based on the residuals after fitting bright sources and searching for a new candidate. To improve the efficiency and accuracy, fitting the PSF models of the faint sources is put as the final step.
7. Check the fitting results. First, each bright source is determined whether it is in quiescence. Second, the information of a candidate is checked. If there is a candidate with  $S/N > 3$  and the flux is higher than the sensitivity, a visual inspection will be carefully performed to determine the credibility.

Figure 5 displays an example of the final light curve fitting result of LE (2–6 keV) based on method 1. The left panel is the corresponding scanning tracks. Thirteen bright sources are monitored in this observation, and their information is listed in Table 3. In the right panel, the blue lines represent light curves after the background is subtracted and GTI is selected. The red solid lines refer to the final fitting results of the bright sources in the three groups, and the grey lines are the corresponding residuals, respectively. Statistically, our fitting result is acceptable.

For most cases, flux information can be obtained unambiguously through method 1. However the X-ray sources are extremely crowded in some regions (such as the galactic center). For these sources, it is sometimes difficult to determine whether the peaks on the light curves are contributed by one or several neighboring sources. Method 1 jointly fits all possible contributing sources simultaneously and acquires the final results based on the returned optimal chi-squared values, which may cause the fluxes of the neighboring sources to interfere with each other. The distance between the sources is the primary interference factor. In addition, the satellite scanning tracks, the GTI coverage, and the fluxes of the target sources during each scanning observation can cause various interference situations. Therefore, further processing is required. The following steps are taken if some neighbors may influence with each other (The target source is denoted as ‘A’):

- Figure out the contaminating neighbors of ‘A’ based on the integral overlap rates of PSF models. To accomplish this, we assume that the complicated case can be

simplified by comparing the overlap of PSF models of two sources in turn, which is defined as:

$$R_{AB} = \frac{\int M_A(t) \cap M_B(t) dt}{\int M_A(t) dt} \times 100\%, \quad (2)$$

and

$$R_{BA} = \frac{\int M_B(t) \cap M_A(t) dt}{\int M_B(t) dt} \times 100\%, \quad (3)$$

where  $M_A(t)$  and  $M_B(t)$  are the PSF models of ‘A’ and ‘B’, respectively. The numerator is the integration of the overlapped PSF models of ‘A’ and ‘B’ over time. If both  $R_{AB}$  and  $R_{BA}$  of each group are higher than 85%, the two sources are considered as coupled with each other in this observation.

- Find the contaminators of ‘A’ in each observational data according to step 1 and exclude the contributions of other sources. Then, fit the flux of ‘A’ individually based on the residuals (This is called method 2).
- Publish the two results and mark the contaminators for the sources in each observational data: result 1 and result 2 (based on method 2).

Taking GX 340+0 as an example, two observational data are selected to illustrate the different mutual interference situations, which are shown in Figures 6 and 7, respectively. In each of the two figures, panel (a) shows the lightcurves and jointly fitting results, and panel (b) represents the corresponding scanning tracks. Panels (c) and (d) are fitting results of GX 340+0 and its contaminators based on methods 1 and 2, respectively. Observably, GX 340+0 are swept by the edges of FOVs during the first observation, while by the center of FOVs during the second one. Meanwhile, the exposures are 242 and 758 s, respectively. Thus, the contaminators of GX340+0 are different in the two observations: the first one has two contaminators while the second one has no contaminators. This is mainly due to the more accurate positioning accuracy when the three FOVs centers cross a source with longer exposure. It is difficult to accurately know the specific contribution of CXOU J164710.2–45521, IGR J16418–4532, and GX 340+0 to the peaks in Figure 6 (c). In this observation, the fluxes of GX 340+0 obtained by methods 1 and 2 are  $0.9 \pm 1.6$  cts/s and  $28.5 \pm 1.6$  cts/s, which are shown in the corresponding panel. The final long-term light curves of GX 340+0 based on the two methods are shown in Figure 8 (a) and (b). Visibly, considerable data points at panel (a) are close to zero, which is probably because the neighboring sources shared the fluxes of GX 340+0. The reason why most of the data points at panel (b) are larger than zero is that method 2 excludes all neighbors of GX 340+0. Panel (c) shows the long-term light

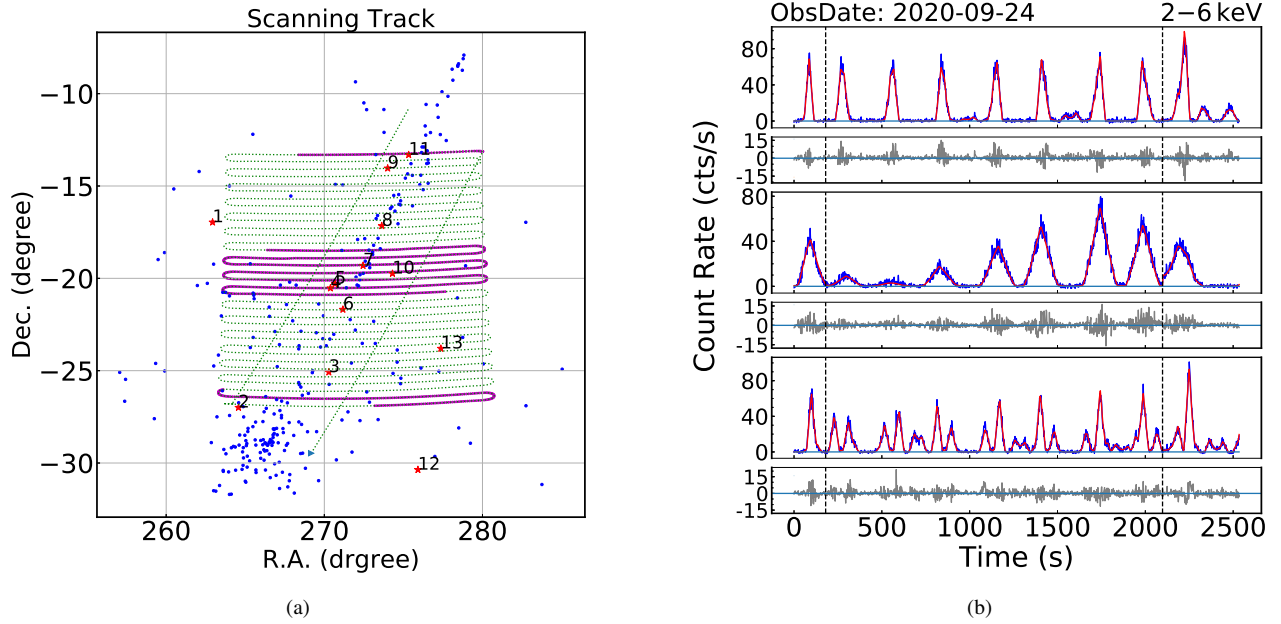


**Figure 5.** Panel (a) shows the corresponding scanned area: The green and purple dashed lines are scanning tracks in the whole observation and those with GTI, respectively. The blue points and red stars denote faint and bright sources in this area. Panel (b) shows an example of light curves at 2–6 keV obtained with LE: The black dashed and red solid lines are segmentations of GTI and the best-fit PSF models of bright sources in the three groups, respectively. The blue and grey solid lines represent clean light curves in this area and residuals, respectively.

**Table 3.** Information of the bright sources in the scanning area shown in Fig 5.

Number	Source Name	R.A.	Dec.	Rate	S/N
(1)	(2)	(deg)	(deg)	(cts s <sup>-1</sup> )	(6)
1	3A 1728 – 169	262.93	–16.96	30.3	23.9
2	SLX 1735 – 269	264.57	–26.99	2.7	5.1
3	GX 5 – 1	270.28	–25.08	127.2	56.3
4	GX 9 + 1	270.38	–20.53	58.1	42.1
5	IGR J18027 – 2016	270.67	–20.29	8.8	6.3
6	HESS J1804 – 216	271.17	–21.68	5.1	4.8
7	AX J1809.8 – 1918	272.45	–19.31	1.4	4.1
8	GX 13 + 1	273.63	–17.16	41.0	14.8
9	GX 17 + 2	274.01	–14.04	74.1	51.5
10	IGR J18172 – 1944	274.31	–19.74	1.5	6.5
11	IGR J18214 – 1318	275.33	–13.31	3.1	4.8
12	H 1820 – 303	275.92	–30.36	41.2	30.9
13	Ginga 1826 – 24	277.37	–23.80	30.8	28.9



curves of GX 340+0 after all uncertain<sup>4</sup> data points are discarded (this is called method 3). In this example, the advantages and disadvantages of the three methods can be seen: 1) method 1 may underestimate the fluxes of some data points; 2) method 2 may overestimate the fluxes of some data points; 3) method 3 retains all convincing results (of which result 1 is consistent with result 2.) but may have fewer data points.

Considering that the radiation of most X-ray sources is mainly concentrated below 6 keV, we perform further processing at 2–4 keV, 4–6 keV, and 2–6 keV for all X-ray sources with neighbors according to method 2.

### 3. GPSS RESULTS

*Insight-HXMT* has performed over 2000 observations since 2017. In GPSS, 1336, 957, and 935 sources are monitored by LE (1–6 keV<sup>5</sup>), ME (7–40 keV) and HE (25–100 keV), respectively. In this section, we present the results of *Insight-HXMT* GPSS and quantify the properties of the three telescopes.

#### 3.1. Catalog

Long-term light curves are essential for understanding the nature of X-ray objects (Hori et al. 2018). They are generally obtained by monitoring and recording fluxes of sources. For each observation, *Insight-HXMT* provides the following information, which is contained in light curves and can be obtained by PSF fitting:

- For known X-ray objects that have crossed the FOVs, their fluxes and S/N at different energy bands are obtained.
- For a new X-ray candidate, its location, flux and S/N are obtained.

Therefore, for *Insight-HXMT*, a source’s long-term variability can be derived by fitting all light curves corresponding to the scanning tracks covering this source. For all monitored sources, the long-term light curves are obtained at 1–100 keV bands. The final results can be accessed on the website of *Insight-HXMT*<sup>6</sup>, and three examples of long-term light curves are shown in Figure 9.

The excess variance ( $F_{\text{rms}}$ ) is an important parameter to characterize the flux variability of a source (Shibazaki & Mit-

suda 1984; Vaughan et al. 2003), so  $F_{\text{rms}}$ <sup>7</sup> at each energy band in this work is calculated to quantify the variability of each source using the following equations:

$$S^2 = \frac{1}{N-1} \sum_i^N (f_i - \bar{f})^2, \quad (4)$$

$$F_{\text{rms}} = \frac{S^2 - \bar{\sigma}^2}{\bar{f}^2}, \quad (5)$$

and

$$dF_{\text{rms}} = \sqrt{\left(\sqrt{\frac{2}{N}} \times \frac{\bar{\sigma}^2}{\bar{f}^2}\right)^2 + \left(\sqrt{\frac{\bar{\sigma}^2}{N}} \times \frac{2\sqrt{F_{\text{rms}}}}{\bar{f}}\right)^2}, \quad (6)$$

where  $N$  is the number of points on each light curve,  $f_i$  is the flux for each observation,  $\bar{\sigma}^2$  is the mean of the square of statistical error, and  $dF_{\text{rms}}$  is the error of  $F_{\text{rms}}$ . The final  $F_{\text{rms}}$  values for monitored sources at different energy bands are listed in our catalog.

Hardness Ratio (HR) is an important parameter that is broadly used to characterize a source’s spectral property (Jin et al. 2006; Sivakoff et al. 2004). It is defined as:

$$\text{HR} = \frac{H}{S}, \quad (7)$$

where  $H$  and  $S$  are count rates in hard and soft energy bands, respectively. According to the error propagation formula, the error of HR is calculated as:

$$\sigma_{\text{HR,stat}} = \frac{H}{S} \sqrt{\frac{\sigma_{\text{S,stat}}^2}{S^2} + \frac{\sigma_{\text{H,stat}}^2}{H^2}}, \quad (8)$$

where  $\sigma_{\text{H,stat}}$  and  $\sigma_{\text{S,stat}}$  are statistic errors of fluxes at H and S bands, respectively. In this paper, HRs are only calculated for sources with averaged S/N higher than 5 both at H and S bands. The averaged S/N are calculated as follows:

$$\bar{f} = \frac{\sum_i \omega_i f_i}{\sum_i \omega_i}, \quad (9)$$

$$\omega_i = \frac{1}{\sigma_i^2}, \quad (10)$$

$$\sigma^2(\bar{f}) = \frac{1}{\left(\sum_i \omega_i\right)^2} \sum_i \omega_i^2 \sigma_i^2 = \frac{1}{\sum_i \frac{1}{\sigma_i^2}}, \quad (11)$$

<sup>4</sup> When the target source interferes with its neighbors, it is impossible to determine whether the flux peaks are contributed by one or several sources. We call the flux of the target source in this observed data ‘uncertain flux’. Such as the fitting result of GX 340+0 in the observation of Figure 6.

<sup>5</sup> Due to the instrument aging of LE, the data at 1–2 keV became inaccurate after August 2020, so all data covering 1–2 keV in this article are the monitored results before August 2020.

<sup>6</sup> <http://hxmtweb.ihep.ac.cn/Transients.jhtml>

<sup>7</sup> If the flux of a source is stable or its statistical error is larger than its variability,  $F_{\text{rms}}$  can be negative, in which case the value of  $F_{\text{rms}}$  is meaningless and marked as  $F_{\text{rms}} < 0$ . It appears that a weak source with averaged flux close to zero and no burst in its long-term light curve may be obtained with a very small or large value of  $F_{\text{rms}}$ , in which case the value may no longer accurately reflect the magnitude of its flux variability.

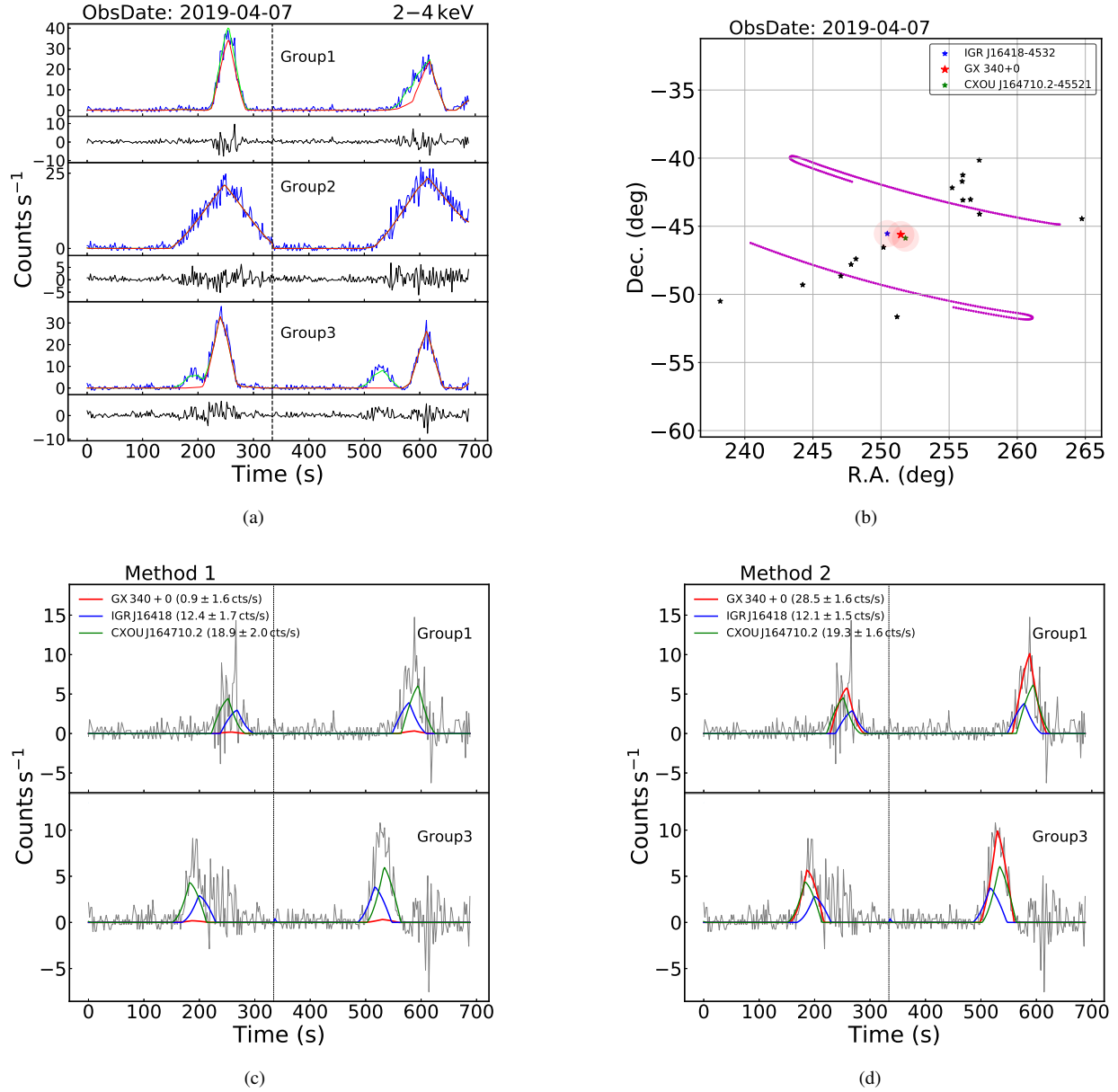


**Figure 6.** The example shows the observational data that GX 340+0 is influenced by its neighbors.

Panel (a) shows the example of light curves that the FOVs crossed GX 340+0. The three blue and green lines are the light curves and the final fitting results (based on method 1) in the three groups of collimator orientation, respectively. The bottom of each group shows the corresponding residuals, and the red lines represent the contributions of sources that do not influence GX 340+0. The vertical black dashed line is the segmentation of GTI. It can be seen that the red and the green lines are consistent in group2, which means the second FOV did not cross GX 340+0 and its contaminants.

Panel (b) shows the corresponding scanning tracks, the location of GX 340+0 and its contaminants in this observation. Each red circle radius is 1°. Colored stars are assigned to sources as follows: Red is GX 340+0. Blue and green are interference sources. Black stars denote bright sources.

Panels (c) and (d) are the fitting results of GX 340+0 and its contaminants based on methods 1 and 2, respectively. The grey lines are the residuals of light curves and contributions of sources that do not influence GX 340+0. Only the results of group1 and group3 are shown because the second FOV did not cross GX 340+0. The fitting results of each source that interferes with the GX 340+0 are marked with colors. The fluxes of the three sources obtained by the two methods are shown with the corresponding legends.

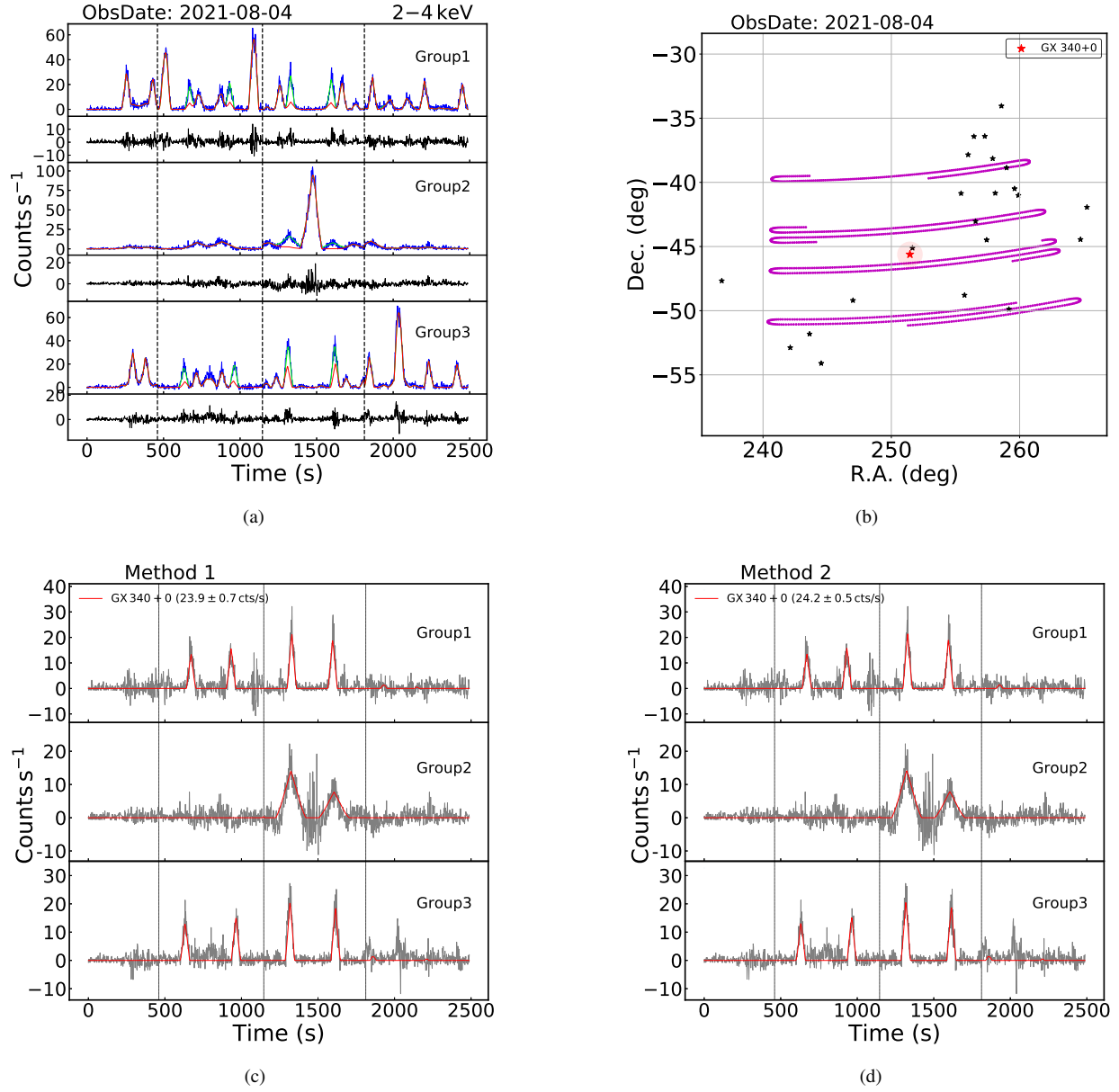


**Figure 7.** The example shows the observational data that GX 340+0 has no contaminants. The figure contents are the same as Figure 6. The obtained fluxes are consistent within errors in panels (c) and (d).

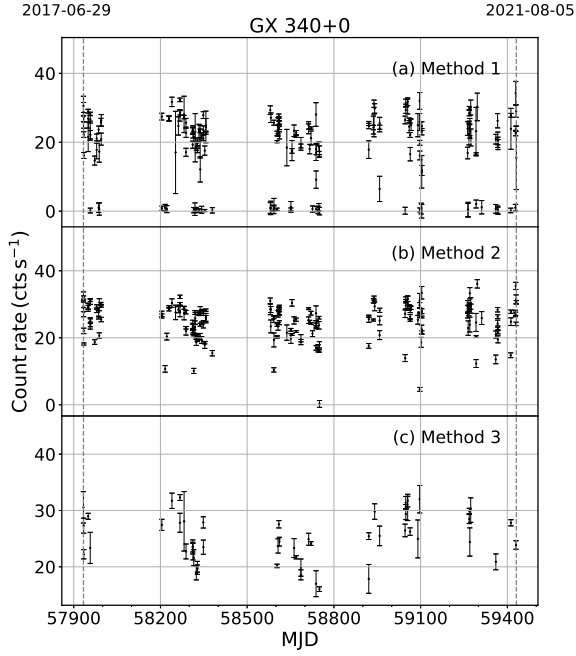


**Figure 8.** The long-term light curves of GX 340+0 at 2–4 keV based on different methods.

and

$$\overline{S/N} = \frac{\bar{f}}{\sigma}, \quad (12)$$

where  $\bar{f}$  and  $f_i$  refer to the averaged flux and the best-fit flux of the  $i$ -th observation, respectively.  $\omega_i$  and  $\sigma_i$  are the corresponding weight and statistical error. Equation (12) is used to calculate the averaged S/N for each source.

We present three *Insight-HXMT* catalogs obtained from the 4 yr GPSS data in the low Galactic latitude sky based on methods 1 - 3, and each catalog contains nine energy bands (1–2 keV, 1–6 keV, 2–4 keV, 2–6 keV, 3–5 keV, 4–6 keV, 5–7 keV, 7–40 keV and 25–100 keV) and the following information: 1) the source names, 2) the source locations, 3) the source types from SIMBAD<sup>8</sup>, 4) the averaged fluxes and corresponding errors at each energy band, 5)  $F_{\text{rms}}$  at each energy band, and 6) HRs and the corresponding errors. To analyze the source properties more accurately, the results in the catalog that correspond to method 3 are utilized in all statistical analyses of this paper. There are 223 sources with  $S/N > 5$  at one or more energy bands among 2–6 keV, 7–40 keV, 25–100 keV (hereafter 2–100 keV), including 59 low mass X-ray binaries (LMXBs), 56 high mass X-ray binaries (HMXBs), 13 supernova remnants (SNRs), 11 pulsars, six Seyfert 1 Galaxies, 23 other type sources, and 55 unclas-

<sup>8</sup> <http://simbad.u-strasbg.fr/simbad/>

It is worth noting that, in this paper, the source type of MAXIJ1348–630 and Swift J0243.6+6124 are adopted from Carotenuto et al. (2022) and Chakrabarty (2018) rather than the SIMBAD database.

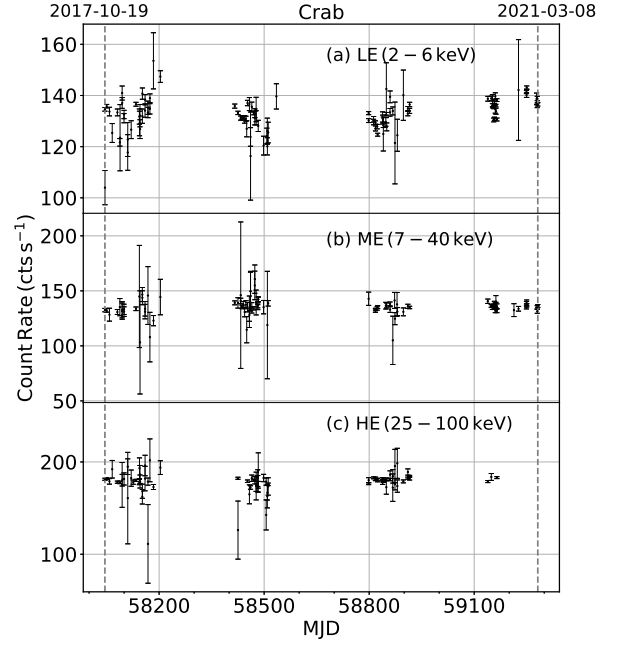


**Figure 9.** The long-term light curves of Crab at 2–6 keV, 7–40 keV, 25–100 keV obtained with LE, ME and HE, respectively.

sified sources. Their information at the three energy bands is extracted in Tables 8 - 13, among which the 33 sources marked in blue are bright sources with  $S/N > 5$  at the three energy bands. Moreover, the compact objects of LMXBs and HMXBs are recorded in column (2) of Tables 8 and 9, respectively.

### 3.2. Properties of *Insight-HXMT* Detectors

Conventionally, the long-term light curve of the Crab nebula (hereafter the ‘Crab’) is used to calculate the systematic errors of instruments, because its spectral characteristics are generally stable. Values of systematic errors at different energy bands can be obtained by solving the following equations,

$$\sum_i^N \frac{(f_i - \bar{f})^2}{\sigma_{\text{total},i}^2} = N - 1, \quad (13)$$

$$\sigma_{\text{total},i}^2 = \sigma_{\text{sys}}^2 + \sigma_{\text{stat},i}^2, \quad (14)$$

and

$$\bar{f} = \frac{\sum_i \omega_i f_i}{\sum_i \omega_i}, \quad \omega_i = \frac{1}{\sigma_{\text{total},i}^2}, \quad (15)$$

where  $N$  is the number of observations,  $i$  denotes the  $i$ -th observation.  $\sigma_{\text{total},i}$  is the total error,  $\sigma_{\text{sys}}$  is the systematic error,  $\sigma_{\text{stat},i}$  and  $f_i$  are the statistic error and flux of Crab,  $\omega_i$  is the weight of  $f_i$ , and  $\bar{f}$  is the averaged flux. The systematic errors of all energy bands are listed in Table 4.

The sensitivities at each energy band can be obtained by the S/N-flux relation, which is shown in Figure 10. We assume that the spectra of all detected sources show consistent shapes with Crab's, and their fluxes are obtained in Crab's units. That S/N increases with flux according to statistics is often affected by other factors in reality, such as back-

ground level, exposure time, and effective area. Therefore, by recording the source flux and S/N obtained in each observation, the distribution in Figure 10 is obtained, in which the lowest flux when the corresponding  $S/N = 5$  at each energy band is considered as the sensitivity limit. The details are listed in Table 4.



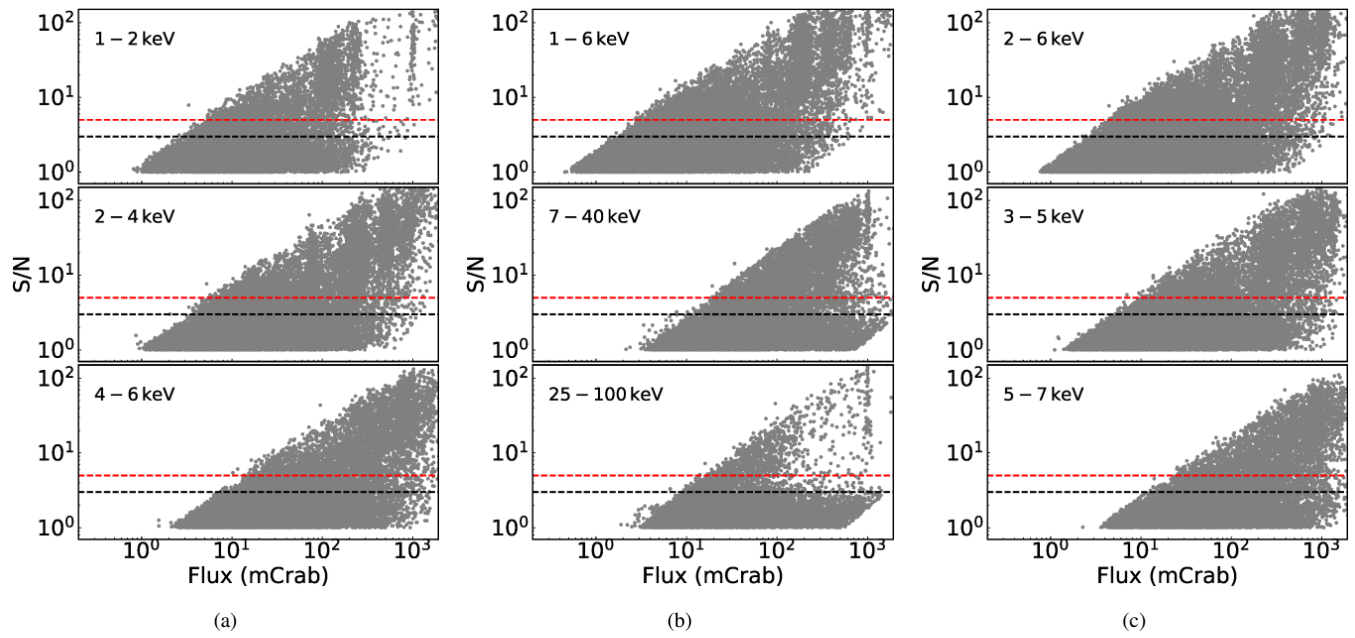


**Figure 10.** This figure shows the relationship between flux and  $S/N$  at nine energy bands. The black and red dashed lines represent  $S/N=3$  and  $S/N=5$ , respectively.

**Table 4.** Properties of *Insight-HXMT* Detectors in Different Energy Band.

	LE							HE	
	1 – 2 keV	2 – 4 keV	4 – 6 keV	2 – 6 keV	3 – 5 keV	5 – 7 keV	1 – 6 keV		7 – 40 keV
$\sigma_{\text{sys}}$ (%)	2.16	3.35	2.61	3.43	3.09	3.49	3.46	1.42	0.83
Source Num. <sup>a</sup>	1337	1345	1342	1343	1343	1343	1336	957	935
Bright Source Num. <sup>b</sup>	261	266	230	294	248	210	268	65	59
Sensitivity1 (mCrab) <sup>c</sup>	4.7	4.6	13.2	4.1	8.9	21.2	2.5	17.6	12.7
Sensitivity1 ( $10^{-10}$ erg s <sup>-1</sup> cm <sup>2</sup> )	0.44	0.40	0.63	0.55	0.55	0.82	0.57	3.16	1.61
Sensitivity2 (mCrab) <sup>d</sup>	0.70	0.69	1.97	0.61	1.33	3.17	0.37	2.35	2.19
Sensitivity2 ( $10^{-11}$ erg s <sup>-1</sup> cm <sup>2</sup> )	0.66	0.60	0.94	0.82	0.82	1.23	0.85	4.21	2.78

NOTE—

<sup>a</sup> The total source number that has been covered at each energy band.<sup>b</sup> One is considered as a bright source when its averaged S/N is higher than 5 and averaged flux is positive.<sup>c</sup> Sensitivity of one scanning observation ( $\sim 2.3$ h).<sup>d</sup> Cumulative sensitivity from June 2017 to August 2021.

#### 4. COMBINE LONG-TERM LIGHT CURVES WITH MAXI

Long-term light curves are essential to reflect the behaviors of X-ray sources, such as their activity duty-cycles and time scales of variability. Providing long-term light curves is one of the main scientific outputs of *Insight-HXMT*. However, the visible duration of each scanned area is limited to a few months per year due to the limitation of the solar angle ( $> 70^\circ$ ), which results in gaps in long-term light curves. With the merged data from other surveys, it is helpful to make up for these gaps. Taking Crab as an instance, Figure 11 shows its long-term light curves that were monitored by *Insight-HXMT*, MAXI<sup>9</sup>, and Swift/BAT<sup>10</sup> from October 2017 to November 2021. It is apparent that *Insight-HXMT* has the advantage of monitoring sources in a wide band, whereas the gaps under its scanning strategy are unavoidable. In comparison, MAXI is an all-sky X-ray monitor and scans the entire sky every 92 minutes, covering the 2–30 keV energy band. MAXI has been monitoring the sky since its launch in 2009 and has accumulated a large amount of continuous observation data. The coded-aperture imager Swift/BAT can cover 88% of the sky each day and has been scanning the sky since its launch (Krimm et al. 2013). Combining the long-term light curves from different missions can reflect more comprehensively the flux variability of X-ray sources in a wider band. In this section, we combine and analyze results at 2–4 keV between *Insight-HXMT* and MAXI, for the reason that the two missions are more sensitive in this energy band and the main radiation energy range of most X-ray sources concentrates in low-energy bands.

##### 4.1. Calibration Analysis

Before combining the data of the two missions, we analyze and calibrate the results of *Insight-HXMT* by comparing the flux at 2–4 keV of the standard Crab model with the actual detection counts. Then the calibrated result is used to check the consistency with the data of MAXI. The top panel of Figure 12 shows the long-term light curves of Crab monitored by the two missions during the same period (from 2017–09–24 to 2021–03–14). One finds that the monitoring time of the two missions is not strictly consistent. Thus the data points of MAXI are interpolated with those of *Insight-HXMT* based on:

$$f_{M,Inter} = f_{M,i} + \frac{t_H - t_{M,i}}{t_{M,i+1} - t_{M,i}} \times (f_{M,i+1} - f_{M,i}), \quad (16)$$

<sup>9</sup> [http://134.160.243.88/star\\_data/J0534+220/J0534+220\\_g\\_lc\\_1\\_orb\\_all.dat](http://134.160.243.88/star_data/J0534+220/J0534+220_g_lc_1_orb_all.dat)

<sup>10</sup> <https://swift.gsfc.nasa.gov/results/transients/Crab.lc.txt>

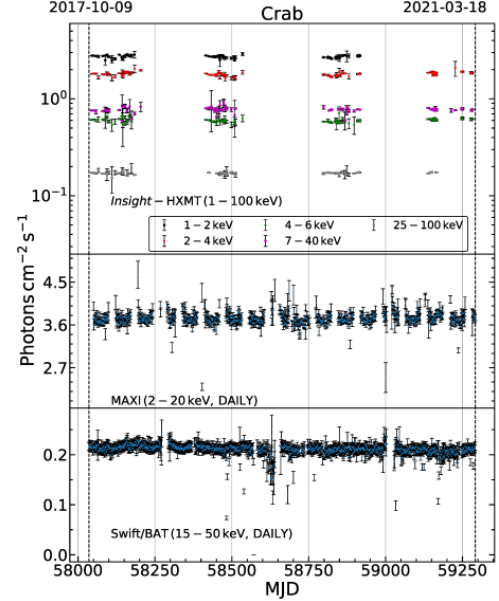


**Figure 11.** Crab light curves from different missions. (Top) Results monitored by *Insight-HXMT* at 1–2 keV, 2–4 keV, 4–6 keV, 7–40 keV and 25–100 keV. (Middle) Results from MAXI at 2–20 keV. (Bottom) Results from Swift/BAT at 15–50 keV. Note that, the Crab light curves of MAXI and Swift/BAT come directly from their webpages, and no additional calibration is done.

and

$$\Delta f_{M,Inter} = \sqrt{\left(\frac{t_{M,i+1} - t_H}{t_{M,i+1} - t_{M,i}}\right)^2 \sigma_{M,i}^2 + \left(\frac{t_H - t_{M,i}}{t_{M,i+1} - t_{M,i}}\right)^2 \sigma_{M,i+1}^2}, \quad (17)$$

where  $f_{M,i}$ ,  $\sigma_{M,i}$  and  $t_{M,i}$  are the flux, flux error, and corresponding MJD for the  $i$ th data point of MAXI, respectively.  $t_H$  is the MJD of *Insight-HXMT* between  $t_{M,i}$  and  $t_{M,i+1}$ . In addition, we can notice that the data points of MAXI are overall higher than those of *Insight-HXMT*. We consider the difference is mainly due to the different adoptions of the standard model of Crab that is used in absolute flux calibration. The absorbed power-law model is adopted in *Insight-HXMT* calibration with a photon index of 2.11, a normalization of  $8.76 \text{ photon cm}^{-2} \text{ s}^{-1} \text{ keV}^{-1}$ , and interstellar absorption  $N_H$  of  $3.6 \times 10^{21} \text{ cm}^{-2}$  (Li et al. 2020). The fluxes (2–4 keV) calculated with this model is  $1.815 \text{ photon s}^{-1} \text{ cm}^{-2}$  and the averaged detected flux is  $1.809 \pm 0.002 \text{ counts s}^{-1} \text{ cm}^{-2}$ . In contrast,  $\Gamma$  and normalization of the spectrum of Crab are assumed as 2.1 and  $10 \text{ photons s}^{-1} \text{ cm}^{-2}$  for MAXI (Hori et al. 2018; Kawamuro et al. 2018; Tomida et al. 2016; Sugizaki et al. 2011). Furthermore, it is written that 1 Crab equals to  $2.2 \text{ photons s}^{-1} \text{ cm}^{-2}$  at 2–4 keV on their webpage<sup>11</sup>. The difference in the selection of normalization is the main reason for the overall difference of the two Crab

<sup>11</sup> [maxi.riken.jp/top/readme.html](http://maxi.riken.jp/top/readme.html)

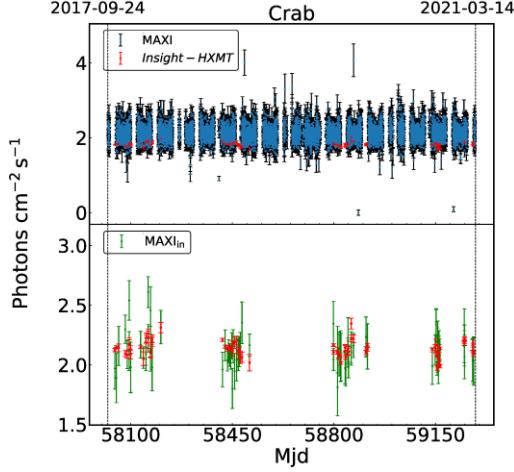


**Figure 12.** (Top) The long-term light curves of Crab that were monitored by MAXI and *Insight-HXMT* at 2–4 keV band during the same period (from 2017-09-24 to 2021-03-14). The red and blue points are monitored results from *Insight-HXMT* and one-orbit time bin results from MAXI, respectively. The vertical errors are the corresponding 1- $\sigma$  statistical uncertainties. (Bottom) The green points and vertical errors are MAXI interpolation data points and corresponding 1- $\sigma$  statistical uncertainties. The red points are calibrated *Insight-HXMT* data points.

light curves in Figure 12. Therefore, a correction factor is needed to calibrate the two missions, and it is derived by dividing the averaged value of interpolated data points of MAXI ( $2.114 \text{ photon cm}^{-2} \text{ s}^{-1}$ ) and the averaged flux of *Insight-HXMT* ( $1.809 \text{ counts s}^{-1} \text{ cm}^{-2}$ ). Consequently, the data points of *Insight-HXMT* are multiplied by 1.17, whose consistency with MAXI is checked based on

$$F_{\text{diff}} = f_M - f_H, \quad (18)$$

and

$$\chi_{\text{diff}}^2 = \sum_{i=1}^N \frac{(f_{M,i} - f_{H,i})^2}{\sigma_{M,i}^2 + \sigma_{H,i}^2}, \quad (19)$$

where  $f_M$  and  $f_H$  are interpolated flux of MAXI and flux from *Insight-HXMT*, respectively.  $\sigma_M$  and  $\sigma_H$  are the corresponding total errors, which are calculated with Equations (13) - (15). The distribution of  $F_{\text{diff}}$  is used to calculate the reduced chi-squared based on Equation (19). Figure 13 shows the Crab light curves and the distribution of  $F_{\text{diff}}$ . The reduced chi-squared is 0.97 for 79 degrees of freedom (DOF), which indicates that the monitored results of Crab by the two missions are consistent.

#### 4.2. Data Combining of the Two Missions

Among the sources with  $S/N > 5$  (at 2–4 keV) in the 4 yr GPSS catalog of *Insight-HXMT*, a total of 131 sources were monitored by both MAXI and *Insight-HXMT*. Their distribution is shown in Figure 14. To obtain more accurate long-term light curves, each source's spectrum is assumed to be

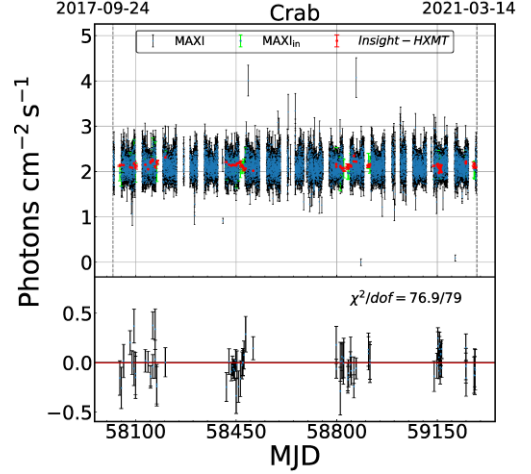


**Figure 13.** (Top) Crab light curves monitored by MAXI and *Insight-HXMT* at 2–4 keV band. The red, blue and green points are calibrated *Insight-HXMT* data points, one-orbit time bin results from MAXI and MAXI interpolation data points, respectively. The vertical errors are the corresponding 1- $\sigma$  statistical uncertainties. (Bottom) The distribution and corresponding 1- $\sigma$  statistical uncertainties of  $F_M - F_H$ . This is used to check the consistency of two satellites, and the reduced chi-squared is 0.97 (dof=79).

an absorbed power-law model with interstellar absorption of  $3.6 \times 10^{21} \text{ cm}^{-2}$ . The power-law models (Equation (20)) with different  $N_0$  and  $-\Gamma$  are used to convolve with the response matrices of *Insight-HXMT* at 2–6 keV, 2–4 keV, and 4–6 keV to obtain the theoretical counts of the corresponding energy band. The calculated results are compared with the detected fluxes at the three energy bands and the model that corresponds to the optimal chi-squared value is determined as the source model. The interstellar absorption is fixed at  $3.6 \times 10^{21} \text{ cm}^{-2}$ , because it has little effect on the fitted flux at 2–4 keV when  $N_H$  is fixed with a value that ranges from  $3.6 \times 10^{20} \text{ cm}^{-2}$  to  $3.6 \times 10^{22} \text{ cm}^{-2}$ . Here we take Crab and Cyg X–1 as examples. Their long-term light curves and the averaged fluxes with  $N_H$  selected as  $3.6 \times 10^{20} \text{ cm}^{-2}$ ,  $3.6 \times 10^{21} \text{ cm}^{-2}$  and  $3.6 \times 10^{22} \text{ cm}^{-2}$  are shown in Figure 15. We find that the averaged fluxes and long-term light curves vary little with different values of  $N_H$ .

$$N(E) = N_0 E^{-\Gamma} e^{-\tau} (\text{cts cm}^{-2} \text{ s}^{-1} \text{ keV}^{-1}). \quad (20)$$

We combine the long-term light curves of the 131 sources and find that  $\sim 70\%$  of the sources match well, while others have reduced chi-squared values larger than 2.5. All the combined results are listed in Table 14. Four typical combined results are shown in Figure 16. One can see that MAXI and *Insight-HXMT* both monitored the outbursts of Swift J0243.6+6124 and EXO 1846–031, which are shown in panels (a) and (b), respectively. Their results are complementary and the combining can provide more complete outburst histories. The data points of EXO 1846–031 moni-

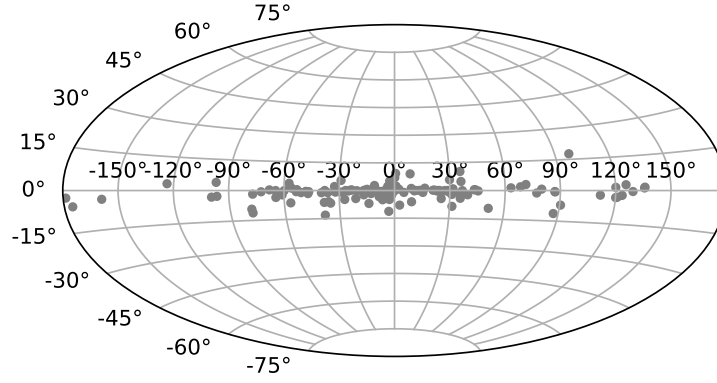


**Figure 14.** Aitoff projection shows the distribution of sources that are used to combine with MAXI.

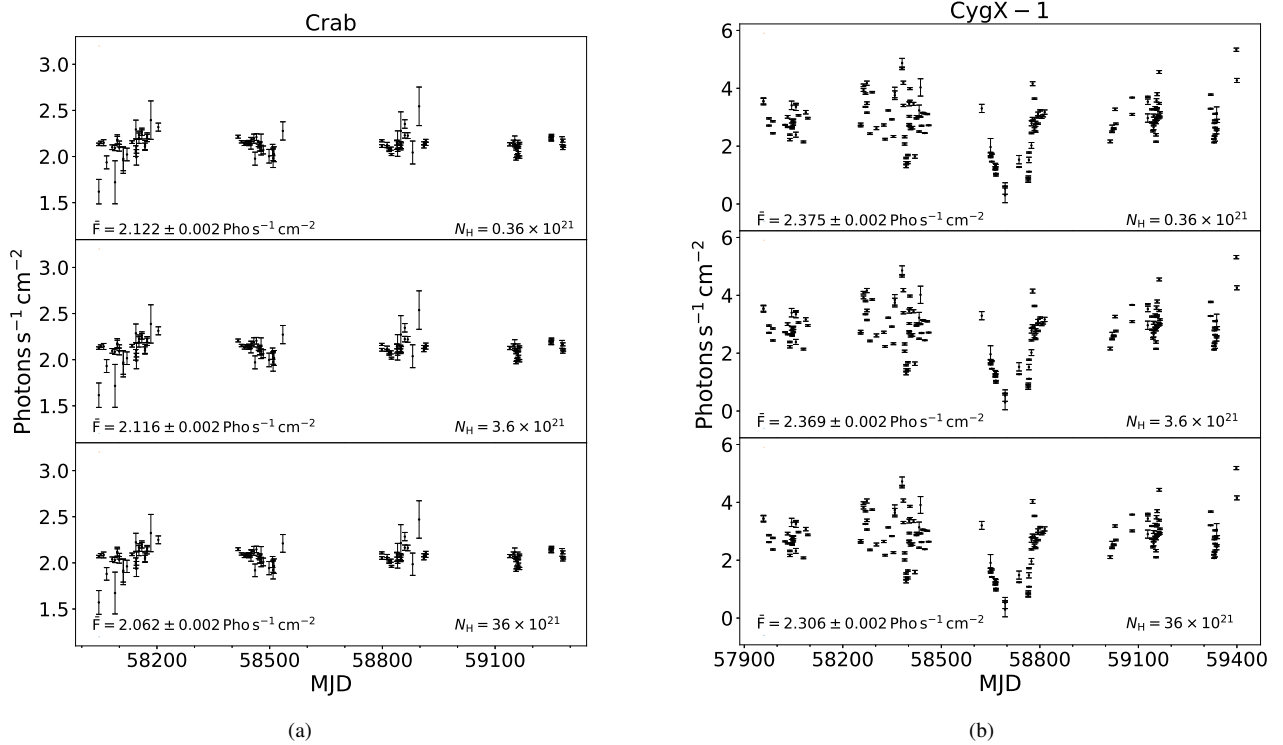


**Figure 15.** The long-term light curves of Crab and Cyg X-1 at 2–4 keV when the interstellar absorption is chosen as  $3.6 \times 10^{20} \text{ cm}^{-2}$ ,  $3.6 \times 10^{21} \text{ cm}^{-2}$  and  $3.6 \times 10^{22} \text{ cm}^{-2}$ , respectively.

tored by the two missions are consistent well within the error bars, while the data for Swift J0243.6+6124 show a large deviation. This is mainly due to a gap in the long-term light curve monitored by MAXI during the outburst phase (MJD 58044 to 58077), while *Insight-HXMT* recorded three flux points during this period. A large deviation is reasonable because the interpolated results cannot accurately restore the outburst lightcurves. It can be seen from panel (c) that the long-term light curve of Cas A monitored by *Insight-HXMT* is overall higher than that of MAXI, which may be due to two reasons. The first one is that Cas A is an extended source

( $\sim 5$  arcmin), and *Insight-HXMT* can record more photons than MAXI due to the larger FOVs. The other possible reason is the complex energy spectrum shape of Cas A is far from the power-law model that is assumed by *Insight-HXMT*. In panel (d), the long-term light curves of GS 1826–24 (also called Ginga 1826–24) that are monitored by the two missions are different from each other as well. That GS 1826–24 is a short time-scale variable source is suspected for their different light curves between the two missions. Because MAXI and *Insight-HXMT* both recorded the averaged flux during their exposures, there may be some differences in



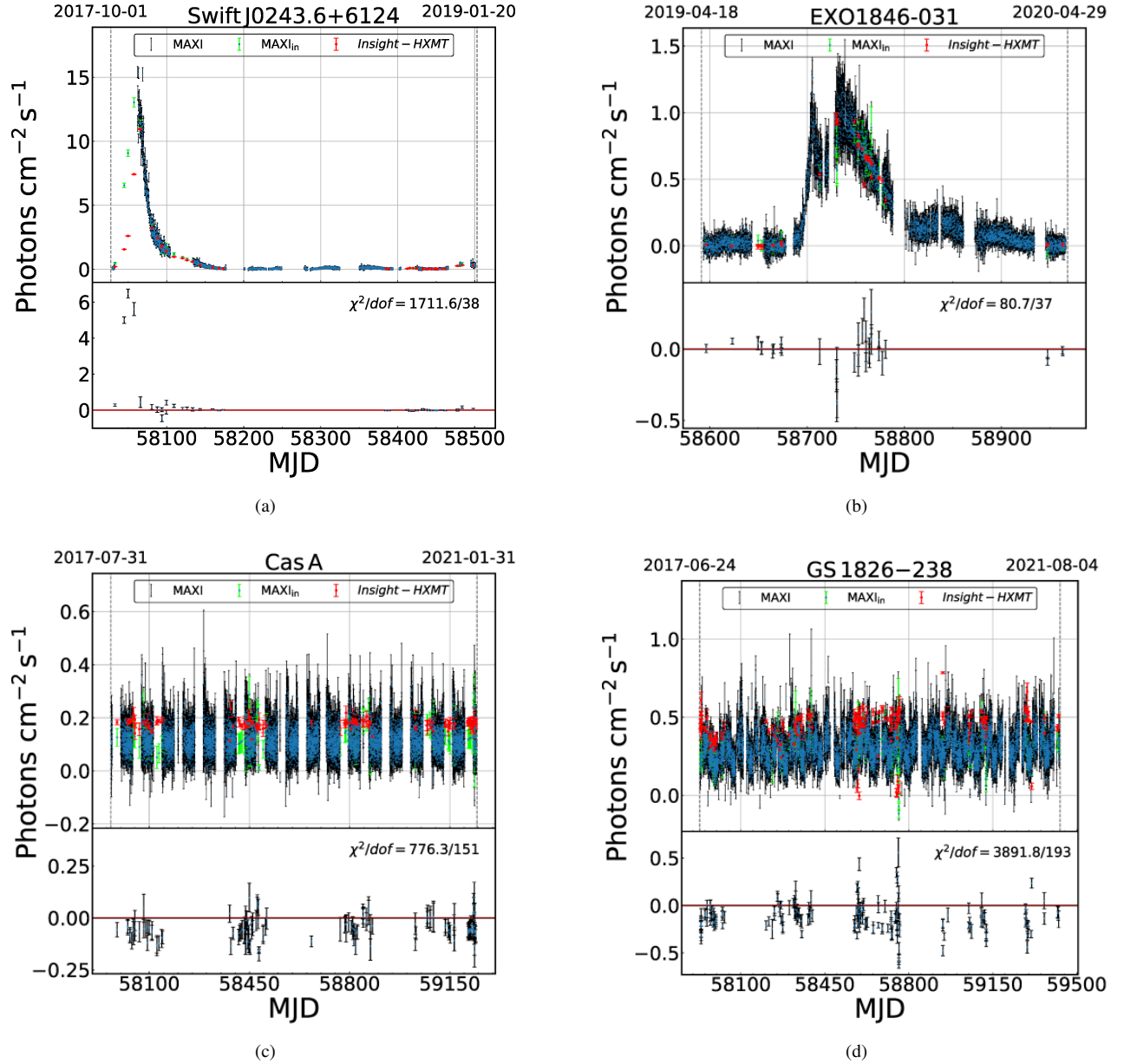


**Figure 16.** Four examples of combined results. The legends for the four panels are the same as those in Figure 13.

the recorded results when the source flux is variable. This can be illustrated briefly by the flux at MJD 58941.85 when *Insight-HXMT* shows the highest flux. The flux monitored by *Insight-HXMT* is  $0.78 \text{ photons s}^{-1} \text{ cm}^{-2}$ , which is 2.5 times that of by MAXI. Figure 17 shows the light curves observed at MJD 58941.85. In this figure, red solid lines are the best fitting results of GS 1826–24 from *Insight-HXMT*, and grey lines are the corresponding residuals. The residuals change from over-fitting to under-fitting, which means that the source was gradually brighter during this observation. Because the flux of each source is considered constant during the exposure, the fitting results mismatch with the light curves in circumstances where the FOVs cross a source with

flux changing. *Insight-HXMT* has the advantage of dealing with such short-timescale variable sources and can obtain a 2-second bin long-term variability of sources based on the light curves and corresponding residuals. The investigation of the short-timescale variable sources by *Insight-HXMT* is beyond the scope of the present work and will be carried out in our following work.

In conclusion, the long-term light curves of some variable sources recorded by both MAXI and *Insight-HXMT* may show differences, which are understandable and acceptable considering their various time scales and different exposures from the two missions. The data combining of the two mis-

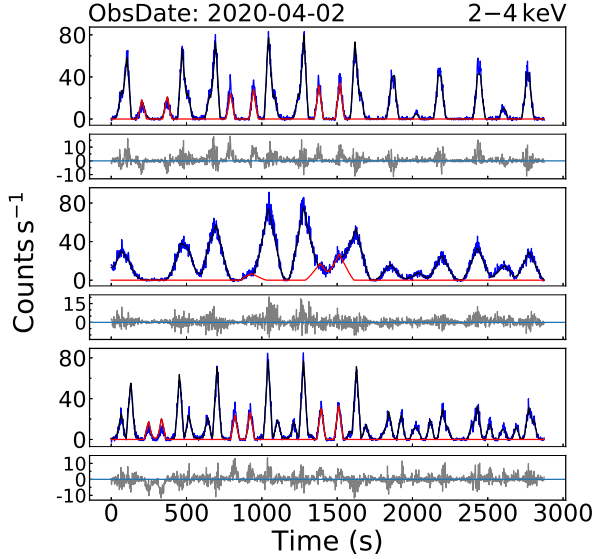


**Figure 17.** The light curves are from *Insight-HXMT* and observed at MJD 58941.85. The blue and black lines are the light curves at 2–4 keV obtained with LE and best-fit results of bright sources. The red lines represent the contribution of GS 1826–24, and grey lines are residuals.

sions has the advantage in providing us with more complete long-term light curves of sources.

## 5. STATISTICAL ANALYSIS

In the previous sections, the fluxes of the monitored sources were obtained at different energy bands. In this section, we statistically analyze the flux variabilities based on  $F_{\text{rms}}$  and calculate HRs to investigate the relations between HRs and the source types, as well as those between HRs and the source spatial distributions.

### 5.1. Flux Variability

We use  $F_{\text{rms}}$  to quantify the flux variability and analyze the properties of the corresponding source types of the 223 sources. When  $F_{\text{rms}} - dF_{\text{rms}}$  of a source is less than or equal to  $F_{\text{rms}}$  of Crab at the corresponding energy band, the source is considered as a flux stable one at that band; otherwise it is a flux variable one. Figure 18 shows the distribution of  $F_{\text{rms}}$  for these sources at 2–6 keV, 7–40 keV and 25–100 keV and the number of flux stable sources is colored in red in each panel. The X-ray binaries in Tables 8 and 9 are LMXBs and HXMBs, respectively. They are classified into neutron star binaries (NSBs) and black hole binaries (BHBs) based on the compact objects. The distributions of their  $F_{\text{rms}}$  are shown in panels (a) and (b). The median  $F_{\text{rms}}$ <sup>12</sup> at different energy bands are utilized to roughly characterize the trend of

$F_{\text{rms}}$ , and they are labeled in Figure 18. As can be seen, the fluxes of HMXBs are more variable than those of LMXBs in the three bands and the fluxes of BHBs are more variable than NSBs at 2–6 keV and 7–40 keV. In addition, the values of  $F_{\text{rms}}$  of LMXBs, NSB, and BHBs tend to decrease as the energy band increases, which are shown in panels (a) and (b). The fluxes of the SNRs, isolated pulsars, and Seyfert 1 galaxies are more stable than those of X-ray binaries. While several sources in the three types have large  $F_{\text{rms}}$ , which may be due to the low averaged fluxes or no detected signals above  $5\sigma$  (Tables 10 - 12).

The 33 bright sources mentioned in Section 3 include 18 LMXBs (16 NSBs and two BHBs), 14 HMXBs (12 NSBs and 2 BHBs), and one SNR (Crab). Because of the low quantity of SNR, we do not analyze it in detail. The flux variability of the rest 32 X-ray binaries are analyzed carefully. Swift J0243.6+6124 is a NS HMXB (Chakrabarty 2018). The outburst was during 2017–2018 and recorded by *Insight-HXMT*. Its long-term light curves at three energy bands are shown in panel (a) of Figure 19, along with the averaged fluxes and  $F_{\text{rms}}$  labelled on the corresponding sub-panels. MAXIJ1348–630 is a BH LMXB classified recently in 2019 (Carotenuto et al. 2022) and has large  $F_{\text{rms}}$  at the three energy bands. Its long-term light curves recorded by *Insight-HXMT* are shown in panel (b) of Figure 19, from which it can be seen that the outburst of MAXIJ1348–630 concentrates in 2019. Figure 20 shows the distribution of  $F_{\text{rms}}$  of all the 32 sources at the three energy bands. It is revealed that the values of  $F_{\text{rms}}$  of 15 NS LMXBs at 2–6 keV are lower than those of 7–40 keV or 25–100 keV in panel (a), and the median  $F_{\text{rms}}$  of LMXBs tends to increase as the energy band increases in panel (c). This is consistent with Mitsuda et al. (1984): the energy spectrum of an NS LMXB is composed of a multicolor spectrum from an optically-thick accretion disk and a blackbody spectrum from the neutron star surface, and the former is radiatively stable, while the latter is highly variable. However, the values of  $F_{\text{rms}}$  of most NS LMXBs at 7–40 keV are not larger than those at 25–100 keV, and even one has  $F_{\text{rms}}$  at 2–6 keV larger than that at 7–40 keV and 25–100 keV. It seems that some NS LMXBs are outliers that the  $F_{\text{rms}}$  at higher energy band is larger than that at lower energy band. However, the fact that both 7–40 keV and 25–100 keV contain the 25–40 keV band and the selection range for the 2–6 keV may lead to inaccurate results. In contrast,  $F_{\text{rms}}$  varies more complicatedly at the three energy bands in HMXBs: (a) The flux variation of HMXBs is more active than that of LMXBs at any of the three energy bands: The values of  $F_{\text{rms}}$  of NS LMXBs are lower than those of NS HMXBs at each energy band, and the values of  $F_{\text{rms}}$  of BH LMXBs are lower than those of BH HMXBs at each energy band; (b)  $F_{\text{rms}}$  of the NS HMXBs shows a tendency to get larger initially and then smaller as

<sup>12</sup> The median  $F_{\text{rms}}$  refers to the middle  $F_{\text{rms}}$  if the data count is odd; otherwise the weighted average of the middle two values of  $F_{\text{rms}}$ .

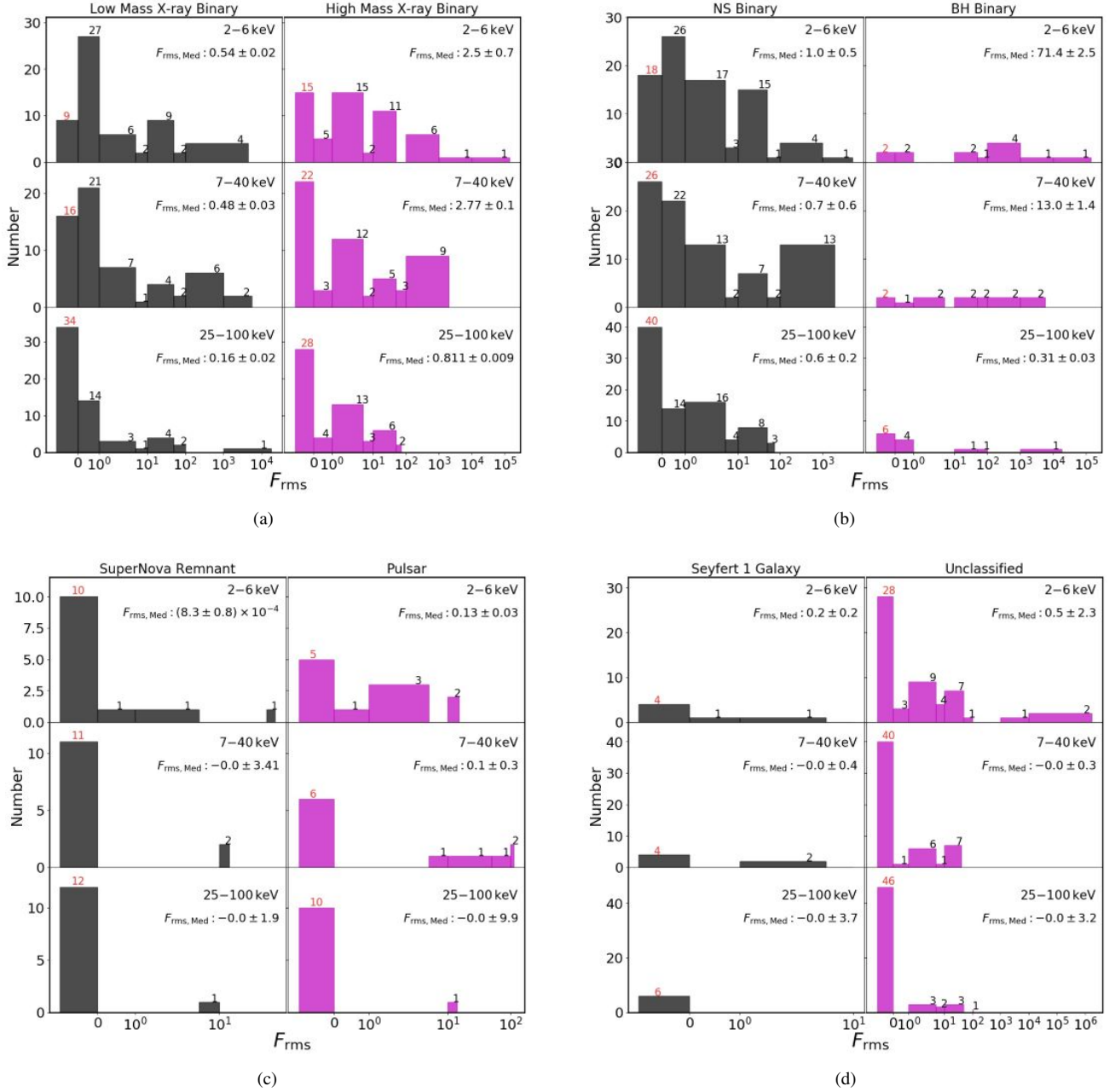


**Figure 18.** The histogram distribution of  $F_{\text{rms}}$  for the sources that have S/N greater than 5 at 2–100 keV. The X and Y axes are the  $F_{\text{rms}}$  and the source number. The number of sources in each  $F_{\text{rms}}$  interval is labelled above the corresponding bar and the red numbers are the number of flux stable sources.

the energy band increases. These may be influenced by the choice of energy bands, although it cannot be excluded that they are related to the accretion processes of the HXMBs. As a binary stellar system is composed of an accreting compact object and an early type massive star, HMXBs can be subdivided into three subclasses according to the differences of companion stars: (a) Be/X ray binaries, (b) supergiant X-ray binaries, (c) supergiant fast X-ray transients. The compact objects in different classes are powered by mass accre-

tion via Roche-lobe overflow or stellar wind capture (Nagase 1989; Sguera et al. 2006), which may lead to more diverse outbreaks.

### 5.2. Estimation of Hardness Ratio (HR)

We calculate HRs of the sources with averaged S/N larger than 5 both at H-band and S-band and statistically study the sources with S/N of HRs larger than 3. The source numbers are 49 and 41 when the S-band is fixed as 2–6 keV and H-

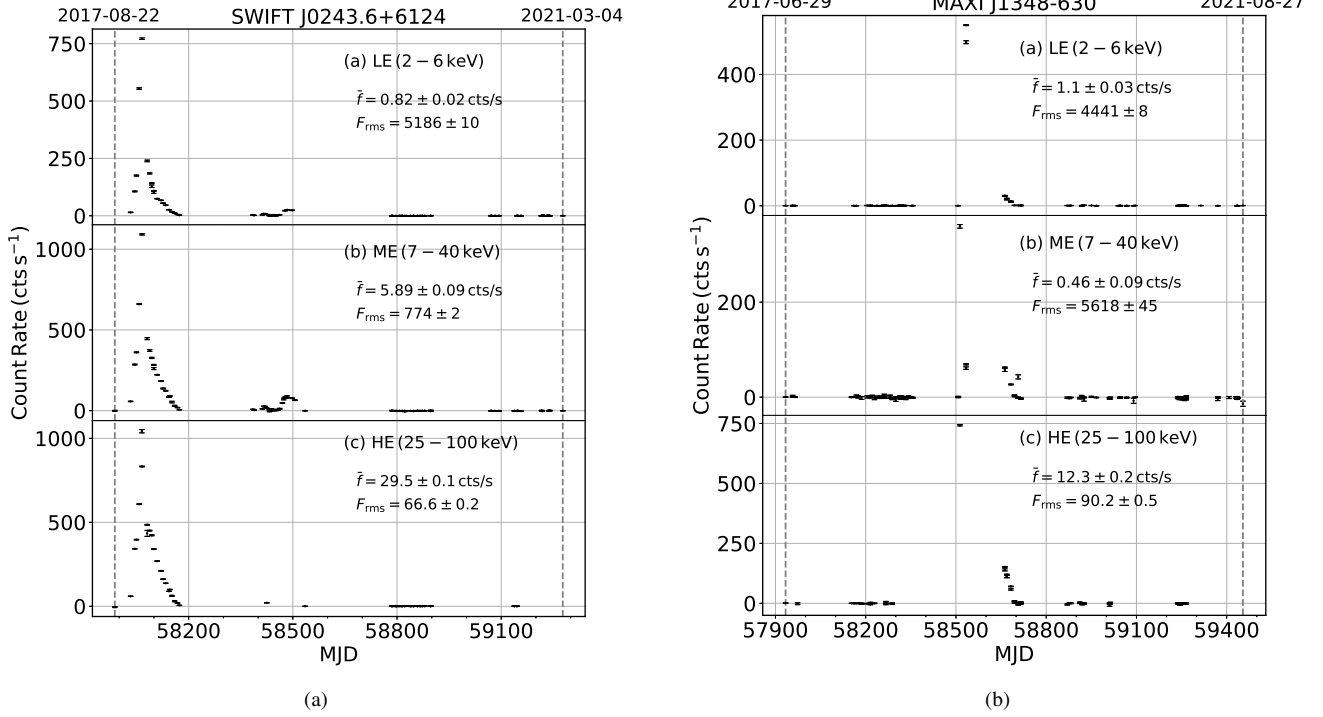


**Figure 19.** The long term light curves of Swift J0243.6+6124 and MAXI J1348-630.

band is selected as 7–40 keV and 25–100 keV, respectively. Their information can be found in Tables 8 - 13.

### 5.2.1. Relations between HRs and $F_{rms}$

The relationship between HRs and the H-band  $F_{rms}$  is investigated. Figure 21 illustrates the HR– $F_{rms}$  relationships for different types of sources, and the corresponding median values of HRs and H-band  $F_{rms}$  are listed in Table 5. The following can be drawn from Figure 21 and Table 5:

- The energy spectra of HMXBs have an overall tendency to be harder than those of LMXBs.
- The fluxes of HMXBs are more variable than those of LMXBs.

The sample sizes for other type of sources are too small to do statistical analysis.

NS and BH binaries are selected for further analysis. Figure 22 shows the relations between their HRs and  $F_{rms}$ , and the corresponding median values are listed in Table 6. We can see that:

- NS LMXBs are spectrally harder than BH LMXBs when H-band is selected as 7–40 keV, while it is the opposite when 25–100 keV is selected for H-band.
- NS HMXBs are spectrally harder than BH HMXBs, no matter which energy band is selected for H-band.

- The fluxes of BH LMXBs are more variable than those of NS LMXBs, while the median  $F_{rms}$  of BH HMXBs are smaller than those of NS HMXBs.

### 5.2.2. Relations between HRs and Source Types

In this part, we investigate the possible relations between HRs and source types. Panels (a) and (b) in Figure 23 show the relations between HR and H-band count rates when H-band is selected as 7–40 keV and 25–100 keV, respectively. It is clear that HMXBs are overall brighter than LMXBs at 25–100 keV, while it is not obvious at 7–40 keV. X-ray binaries (XRBs) dominate a large portion on the galactic plane (Fabbiano 2006), which is the same in the two panels. Thus, only the HRs of HMXBs and LMXBs are analyzed. The relation between their HR and source numbers are shown in Figure 24. The black dashed lines represent HR medians<sup>13</sup>, which are utilized to roughly characterize the trend of HR and are listed in Table 7. Generally, the following conclusions can be drawn:

1. HMXBs are overall spectrally harder than LMXBs, no matter which energy range of H-band is selected.

<sup>13</sup> The median refers to the middle HR if data count is odd; otherwise the weighted average of the middle two HRs.

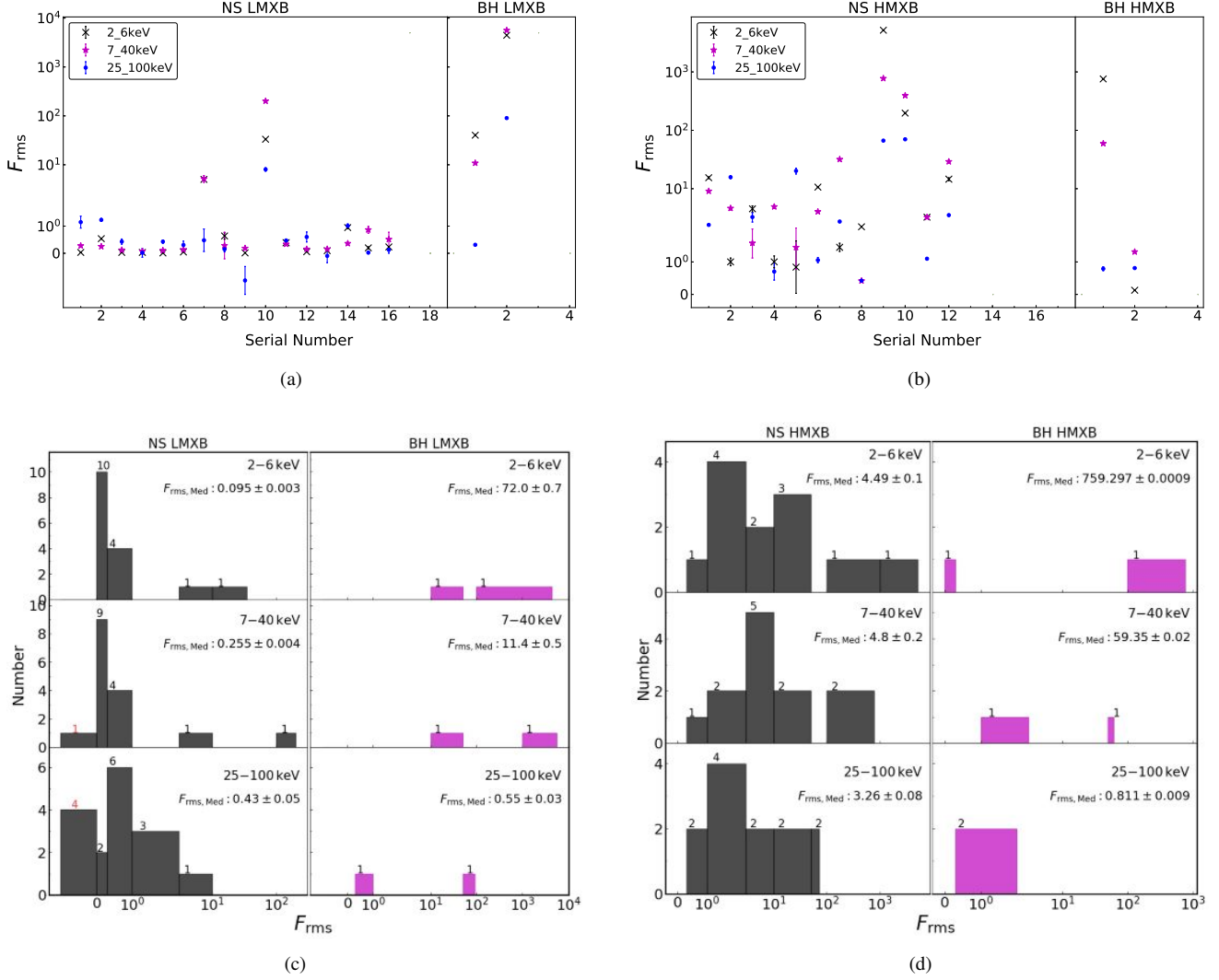


**Figure 20.**  $F_{\text{rms}}$  distribution for the 32 bright X-ray binaries that have  $S/N$  greater than 5 at 2–6 keV, 7–40 keV and 25–100 keV. These sources are classified into LMXB and HMXB based on the mass of donor star and classified into NSB and BHB based on the compact object. The source types and compact objects are labelled on each panel. In panels (a) and (b), the X and Y axes are the serial number and  $F_{\text{rms}}$ , respectively. The black cross, magenta pentagram, and blue points represent the  $F_{\text{rms}}$  at 2–6 keV, 7–40 keV, and 25–100 keV for each source, respectively. Vertical error bars represent the error of the  $F_{\text{rms}}$ . Panels (c) and (d) are the corresponding histograms of (a) and (c).

2. The HR medians of LMXBs and HMXBs become softer as a harder energy range of the H-band is selected.

## 6. SUMMARY AND CONCLUSION

We have presented the first *Insight-HXMT* catalog at low Galactic latitudes, based on the 4 yr GPSS data mainly at 2–6 keV (LE), 7–40 keV (ME), and 25–100 keV (HE) bands. The limiting sensitivities of 0.61 mCrab, 2.35 mCrab and 2.19 mCrab are achieved and 1343, 957, and 935 sources have been monitored up to August 2021 at 2–6 keV (LE), 7–40 keV (ME), and 25–100 keV (HE), respectively.

Combining data from different missions can provide more complete long-term light curves, which are useful to study the nature of these sources. The long-term light curves at 2–4 keV are used to combine with those from MAXI. The light curves of *Insight-HXMT* and MAXI for most sources are consistent well with each other, while some show differences. Two main reasons resulting in those differences are investigated. The first reason comes from the difference in the size of the FOVs of the two missions, which may lead to the different number of photons received from the extended source (such as Cas A). The other reason is that an object is a short-time scale variable source, for which *Insight-HXMT* and MAXI both recorded the averaged fluxes. *Insight-HXMT*



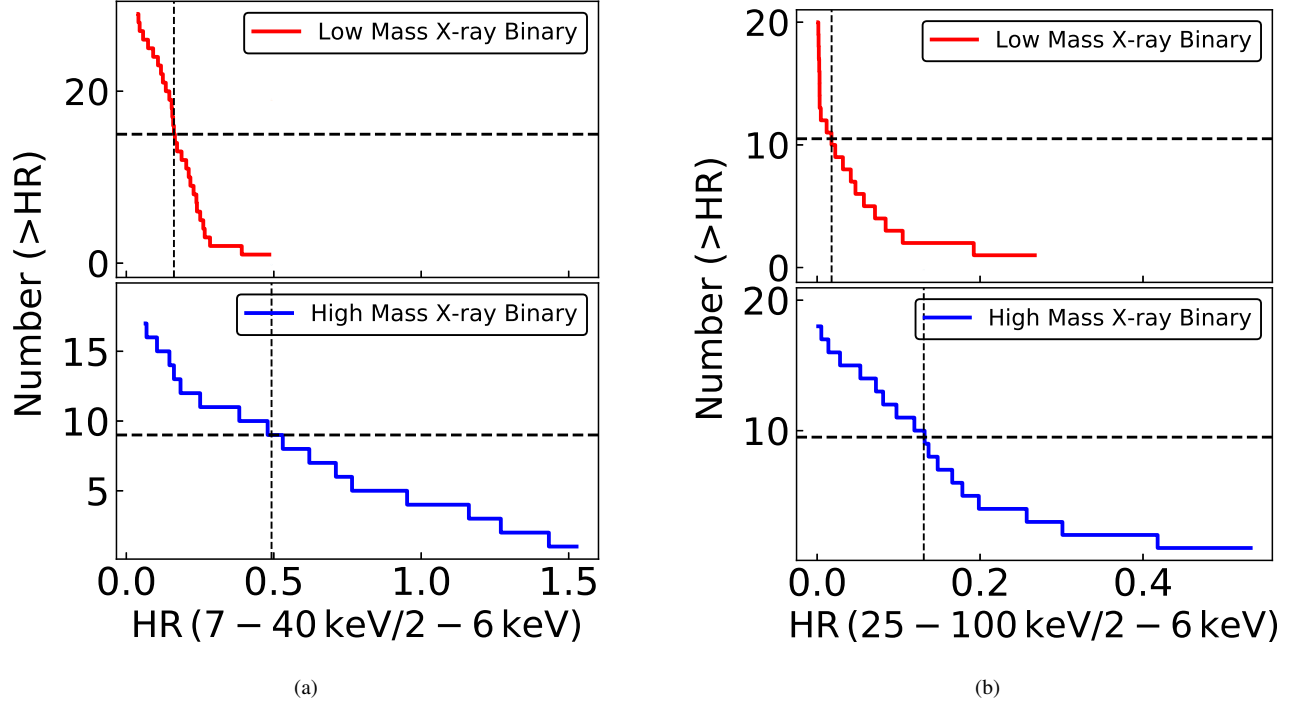


**Figure 21.** The relations between HRs and  $F_{\text{rms}}$ . H-band is selected as 7–40 keV in panel (a) and 25–100 keV in panel (b).

**Table 5.** The Median Value of HR and that of H-band  $F_{\text{rms}}$  (S band: 2–6 keV).

H-band	LMXB	HMXB	Pulsar	SNR	Seyfert1	Cluster of Galaxies	Unclassified
(1)	(2)	(3)	(4)	(5)	(6)	(7)	(8)
$\text{HR}_{7-40 \text{ keV}}$	$0.163 \pm 0.007$	$0.5 \pm 0.2$	–	$0.3193 \pm 0.0007$	–	$0.17 \pm 0.02$	$0.16 \pm 0.02$
$F_{\text{rms},7-40 \text{ keV}}$	$0.35 \pm 0.03$	$4.05 \pm 0.07$	–	$0.0002 \pm 0.0002$	–	$1.5 \pm 0.6$	$1.01 \pm 0.06$
$\text{HR}_{25-100 \text{ keV}}$	$0.017 \pm 0.001$	$0.13 \pm 0.01$	$0.031 \pm 0.005$	$0.072 \pm 10^{-4}$	$0.11 \pm 0.03$	–	–
$F_{\text{rms},25-100 \text{ keV}}$	$0.43 \pm 0.05$	$2.4 \pm 0.04$	$< 0$	$< 0$	$< 0$	–	–

NOTE—

– represents there is no this type of source.

**Table 6.** The Median Value of HR and that of H-band  $F_{\text{rms}}$  (S band: 2–6 keV).

H-band	NS LMXB	BH LMXB	NS HMXB	BH HMXB
(1)	(2)	(3)	(4)	(5)
$\text{HR}_{7-40 \text{ keV}}$	$0.1988 \pm 0.0009$	$0.0413 \pm 0.0007$	$0.66 \pm 0.02$	$0.0733 \pm 0.0004$
$F_{\text{rms},7-40 \text{ keV}}$	$0.3 \pm 0.5$	$118 \pm 1$	$4.08 \pm 0.07$	$1.4 \pm 0.02$
$\text{HR}_{25-100 \text{ keV}}$	$0.011 \pm 0.001$	$0.194 \pm 0.003$	$0.14 \pm 0.005$	$0.01637 \pm 8 \times 10^{-5}$
$F_{\text{rms},25-100 \text{ keV}}$	$0.43 \pm 0.05$	$0.55 \pm 0.03$	$2.74 \pm 0.08$	$0.811 \pm 0.009$

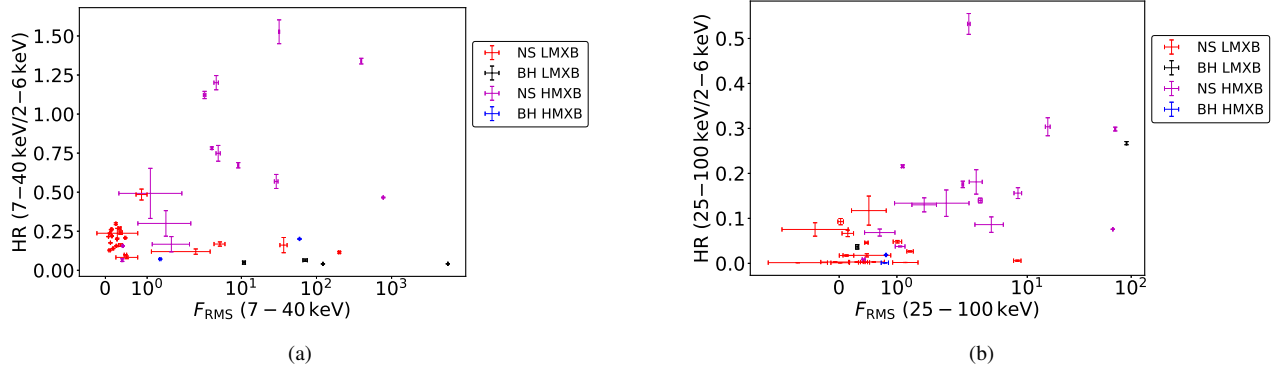


**Figure 22.** The relations between HRs and  $F_{\text{rms}}$  for NS and BH binaries.

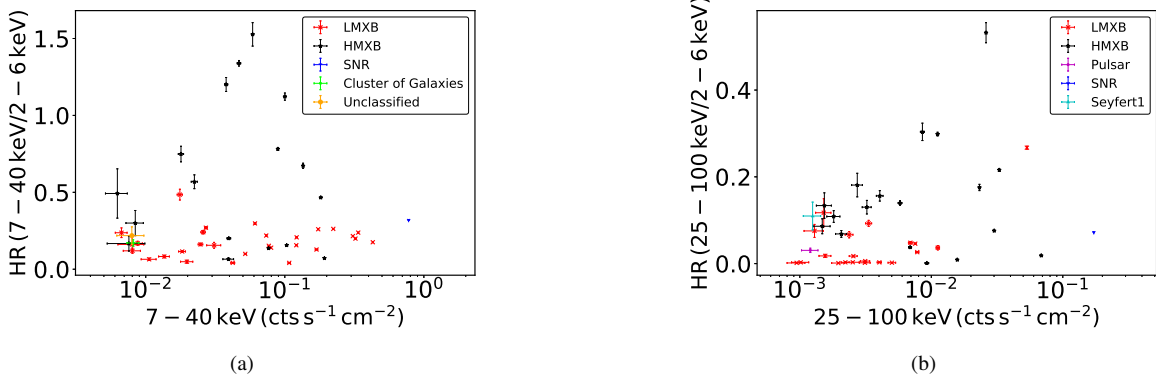


**Figure 23.** The relations between HR and H-band count rates. A color is assigned to each source type.

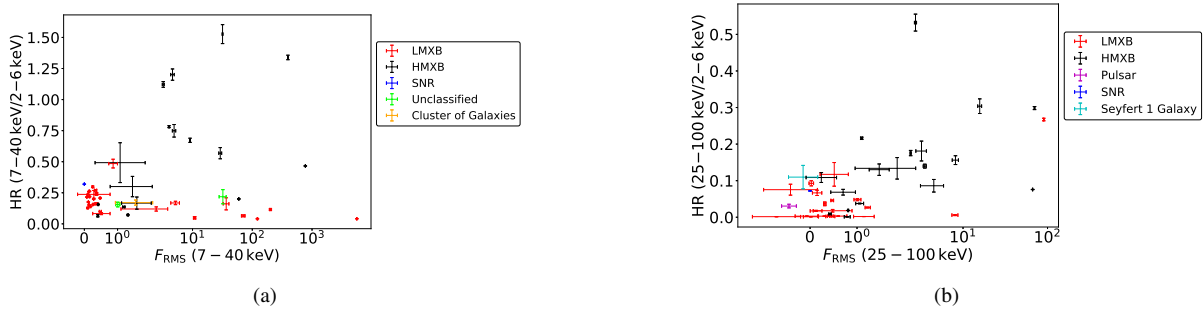


**Figure 24.** This figure shows the relations between the cumulative numbers and HRs. X-axis is HR, and Y-axis is the count of sources higher than the value corresponding to X-axis. The black dashed lines are the median values of HRs.

**Table 7.** The Median Value of HR (S band: 2–6 keV).

H band	HMXB	LMXB
7 – 40 keV	$0.5 \pm 0.2$	$0.161 \pm 0.008$
25 – 100 keV	$0.13 \pm 0.01$	$0.018 \pm 0.001$

has advantages in observing short-time scale sources thanks to its large FOVs and scanning strategy.

The 4-year catalog contains 223 sources with S/N greater than 5 at 2–100 keV and 33 sources with S/N greater than 5 at 2–6 keV, 7–40 keV, and 25–100 keV. We have analyzed the flux variabilities for these sources based on their  $F_{\text{rms}}$ , and investigated the relations between  $F_{\text{rms}}$  and the source types, and between  $F_{\text{rms}}$  and HRs. The following conclusions are drawn:

- During the GPSS of *Insight-HXMT*, most of the SNRs are flux stable. The fluxes of most isolated pulsars and Seyfert 1 Galaxies vary little or are about zero.
- The fluxes of BHBs are more variable than those of NSBs.
- Most of the values of  $F_{\text{rms}}$  of NS LMXBs at 2–6 keV are lower than those at higher energy bands, which may be related to the composition of the energy spectra of NS LMXBs.
- $F_{\text{rms}}$  of HMXBs varies more complicatedly at different energy bands, which may be due to the complicated accretion processes of HMXBs.

- The fluxes of BH LMXBs at 7–40 keV have an overall tendency to be more variable than those of NS LMXBs at the same band, but their HRs (7–40 keV / 2–6 keV) have a softer tendency than NS LMXBs.

- The NS HMXBs not only have more variable fluxes than NS LMXBs, but also have harder spectra than NS LMXBs (S-band: 2–6 keV; H-band: 7–40 keV or 25–100 keV).

We have studied the relations between HRs and source types. It is found that HMXBs are generally harder than LMXBs, and as a harder energy range of the H-band is selected, the HR of X-ray binaries tends to become softer.

Chen Wang thank Zeming Zhou and Yufeng Li for their advice and help on improving the manuscript. We thank the referee for her/his pertinent comments and suggestions that helped to improve the quality of our paper. This work made use of the data from the *Insight-HXMT* mission, a project funded by China National Space Administration (CNSA) and the Chinese Academy of Sciences (CAS). The authors thank supports from the National Natural Science Foundation of China under Grants Nos.U1838202, U1838201, U1838105, U1838107, U1838113, the Youth Innovation Promotion Association of the CAS (grant id 2018014), and the National Key R&D Program of China (Grant No. 2021YFA0718500). This work was partially supported by International Partnership Program of Chinese Academy of Sciences (Grant No.113111KYSB20190020).

## REFERENCES

- Boller, T., Freyberg, M. J., Trümper, J., et al. 2016, *A&A*, 588, A103, doi: [10.1051/0004-6361/201525648](https://doi.org/10.1051/0004-6361/201525648)
- Burrows, D. N., Hill, J. E., Nousek, J. A., et al. 2005, *SSRv*, 120, 165, doi: [10.1007/s11214-005-5097-2](https://doi.org/10.1007/s11214-005-5097-2)
- Cao, X., Jiang, W., Meng, B., et al. 2019, arXiv e-prints, arXiv:1910.04451. <https://arxiv.org/abs/1910.04451>
- Carotenuto, F., Corbel, S., & Tzioumis, A. 2022, *MNRAS*, 517, L21, doi: [10.1093/mnras/slac087](https://doi.org/10.1093/mnras/slac087)
- Chakrabarty, D. 2018, in American Astronomical Society Meeting Abstracts, Vol. 231, American Astronomical Society Meeting Abstracts #231, 160.04
- Chen, Y., Cui, W., Li, W., et al. 2020, *Science China Physics, Mechanics, and Astronomy*, 63, 249505, doi: [10.1007/s11433-019-1469-5](https://doi.org/10.1007/s11433-019-1469-5)
- Evans, P. A., Page, K. L., Osborne, J. P., et al. 2020, *ApJS*, 247, 54, doi: [10.3847/1538-4365/ab7db9](https://doi.org/10.3847/1538-4365/ab7db9)
- Fabbiano, G. 2006, *ARA&A*, 44, 323, doi: [10.1146/annurev.astro.44.051905.092519](https://doi.org/10.1146/annurev.astro.44.051905.092519)
- Forman, W., Jones, C., Cominsky, L., et al. 1978, *ApJS*, 38, 357, doi: [10.1086/190561](https://doi.org/10.1086/190561)
- Forman, W., Jones, C., Tananbaum, H., et al. 1973, *ApJL*, 182, L103, doi: [10.1086/181229](https://doi.org/10.1086/181229)
- Giacconi, R., Kellogg, E., Gorenstein, P., Gursky, H., & Tananbaum, H. 1971, *ApJL*, 165, L27, doi: [10.1086/180711](https://doi.org/10.1086/180711)
- Giacconi, R., Branduardi, G., Briel, U., et al. 1979, *ApJ*, 230, 540, doi: [10.1086/157110](https://doi.org/10.1086/157110)
- Hori, T., Shidatsu, M., Ueda, Y., et al. 2018, *ApJS*, 235, 7, doi: [10.3847/1538-4365/aaa89c](https://doi.org/10.3847/1538-4365/aaa89c)

- HSDC. 2020, The HXMT Data Reduction Guide (v2.01), <http://hxmtweb.ihep.ac.cn/SoftDoc/66.jhtml>
- Jin, Y. K., Zhang, S. N., & Wu, J. F. 2006, *ApJ*, 653, 1566, doi: 10.1086/508677
- Kawamuro, T., Ueda, Y., Shidatsu, M., et al. 2018, *ApJS*, 238, 32, doi: 10.3847/1538-4365/aad1ef
- Krimm, H. A., Holland, S. T., Corbet, R. H. D., et al. 2013, *ApJS*, 209, 14, doi: 10.1088/0067-0049/209/1/14
- Krivonos, R., Sazonov, S., Kuznetsova, E., et al. 2021, arXiv e-prints, arXiv:2111.02996. <https://arxiv.org/abs/2111.02996>
- Levine, A. M., Lang, F. L., Lewin, W. H. G., et al. 1984, *ApJS*, 54, 581, doi: 10.1086/190944
- Li, G., Wu, M., Zhang, S., & Jin, Y.-K. 2009, *ChA&A*, 33, 333, doi: 10.1016/j.chinastron.2009.07.013
- Li, X., Li, X., Tan, Y., et al. 2020, *Journal of High Energy Astrophysics*, 27, 64, doi: 10.1016/j.jheap.2020.02.009
- Liao, J.-Y., Zhang, S., Chen, Y., et al. 2020, *Journal of High Energy Astrophysics*, 27, 24, doi: 10.1016/j.jheap.2020.02.010
- Liu, C., Zhang, Y., Li, X., et al. 2020, *Science China Physics, Mechanics, and Astronomy*, 63, 249503, doi: 10.1007/s11433-019-1486-x
- Long, K. S., Helfand, D. J., & Grabelsky, D. A. 1981, *ApJ*, 248, 925, doi: 10.1086/159222
- Matsuoka, M., Kawasaki, K., Ueno, S., et al. 2009, *PASJ*, 61, 999, doi: 10.1093/pasj/61.5.999
- Mitsuda, K., Inoue, H., Koyama, K., et al. 1984, *PASJ*, 36, 741
- Morhác, M., Kliman, J., Matoušek, V., Veselský, M., & Turzo, I. 1997, *Nuclear Instruments and Methods in Physics Research A*, 401, 113, doi: 10.1016/S0168-9002(97)01023-1
- Nagase, F. 1989, *PASJ*, 41, 1
- Nang, Y., Liao, J.-Y., Sai, N., et al. 2020, *Journal of High Energy Astrophysics*, 25, 39, doi: 10.1016/j.jheap.2020.01.002
- Nugent, J. J., Jensen, K. A., Nousek, J. A., et al. 1983, *ApJS*, 51, 1, doi: 10.1086/190838
- Pavlinisky, M., Sazonov, S., Burenin, R., et al. 2022, *A&A*, 661, A38, doi: 10.1051/0004-6361/202141770
- Revnitsev, M., Sazonov, S., Jahoda, K., & Gilfanov, M. 2004, *A&A*, 418, 927, doi: 10.1051/0004-6361:20035798
- Reynolds, A. P., Parmar, A. N., Hakala, P. J., et al. 1999, *A&AS*, 134, 287, doi: 10.1051/aas:1999140
- Ryan, C. G., Clayton, E., Griffin, W. L., Sie, S. H., & Cousins, D. R. 1988, *Nuclear Instruments and Methods in Physics Research B*, 34, 396, doi: 10.1016/0168-583X(88)90063-8
- Sai, N., Liao, J.-Y., Li, C.-K., et al. 2020, *Journal of High Energy Astrophysics*, 26, 1, doi: 10.1016/j.jheap.2020.02.005
- Seward, F. D. 1982, *Advances in Space Research*, 2, 153, doi: 10.1016/0273-1177(82)90266-6
- Sguera, V., Bazzano, A., Bird, A. J., et al. 2006, *ApJ*, 646, 452, doi: 10.1086/504827
- Shibazaki, N., & Mitsuda, K. 1984, in *American Institute of Physics Conference Series*, Vol. 115, *High Energy Transients in AstroPhysics*, ed. S. E. Woosley, 63–71, doi: 10.1063/1.34571
- Sivakoff, G. R., Sarazin, C. L., & Carlin, J. L. 2004, *ApJ*, 617, 262, doi: 10.1086/425244
- Sugizaki, M., Mihara, T., Serino, M., et al. 2011, *PASJ*, 63, S635, doi: 10.1093/pasj/63.sp3.S635
- Tomida, H., Uchida, D., Tsunemi, H., et al. 2016, *PASJ*, 68, S32, doi: 10.1093/pasj/psw006
- Truemper, J. 1982, *Advances in Space Research*, 2, 241, doi: 10.1016/0273-1177(82)90070-9
- Vaiana, G. S. 1990, in *Imaging X-Ray Astronomy. A Decade of Einstein Observatory Achievements*, ed. M. Elvis, 61
- van Speybroeck, L., Epstein, A., Forman, W., et al. 1979, *ApJL*, 234, L45, doi: 10.1086/183106
- Vaughan, S., Edelson, R., Warwick, R. S., & Uttley, P. 2003, *MNRAS*, 345, 1271, doi: 10.1046/j.1365-2966.2003.07042.x
- Voges, W., Aschenbach, B., Boller, T., et al. 1999, *A&A*, 349, 389, <https://arxiv.org/abs/astro-ph/9909315>
- Warwick, R. S., Marshall, N., Fraser, G. W., et al. 1981, *MNRAS*, 197, 865, doi: 10.1093/mnras/197.4.865
- Wood, K. S., Meekins, J. F., Yentis, D. J., et al. 1984, *ApJS*, 56, 507, doi: 10.1086/190992
- Xie, F., Zhang, J., Song, L.-M., Xiong, S.-L., & Guan, J. 2015, *Ap&SS*, 360, 13, doi: 10.1007/s10509-015-2559-1
- XMMSL2. 2017, THE XMM-NEWTON SLEW SURVEY SOURCE CATALOGUE:XMMSL2, <https://www.cosmos.esa.int/web/xmm-newton/xmmsl2-ug#AimsCat>
- Zhang, S.-N., Li, T., Lu, F., et al. 2020, *Science China Physics, Mechanics, and Astronomy*, 63, 249502, doi: 10.1007/s11433-019-1432-6

APPENDIX

A. CATALOG OF THE BRIGHT SOURCES AND THE COMBINED RESULTS WITH MAXI

**Table 8.** The First Four-year GPSS Catalog of *Insight-HXMT* (Low Mass X-ray Binary).

Source name	Compact object	R.A. (deg)	Dec. (deg)	$R_{2-6\text{ keV}}$ cts s $^{-1}$	$R_{7-40\text{ keV}}$ cts s $^{-1}$	$R_{25-100\text{ keV}}$ cts s $^{-1}$	$F_{\text{rms}1^c}$	$F_{\text{rms}2^d}$	$F_{\text{rms}3^e}$	HR1 $^e$	HR2 $^b$
(1)	(2)	(3)	(4)	(5)	(6)	(7)	(8)	(9)	(10)	(11)	(12)
GX 349 + 2	NS	256.43	-36.42	89.3 ± 0.1	54.9 ± 0.1	2.0 ± 0.1	0.0315 ± 0.0008	0.279 ± 0.004	1.1 ± 0.2	0.1988 ± 0.0009	0.0019 ± 0.0002
IGR J17091 - 3624	BH	257.28	-36.41	1.9 ± 0.2	< 0.5	< 0.1	71 ± 2	596 ± 44	< 0	< 0.16	< 0.11
SAX J1712.6 - 3739	NS	258.14	-37.64	0.36 ± 0.05	< 0.3	< 0.6	12 ± 1	1970 ± 316	23 ± 23	< 0.24	< 0.08
IGR J17254 - 3257	NS	261.35	-32.95	0.21 ± 0.03	< -0.22	< 0.5	11 ± 2	1.7 ± 1.0	< 0	< 0.43	< 0.07
3A 1728 - 169	-	262.93	-16.96	28.48 ± 0.06	12.6 ± 0.1	< 1.9	0.0075 ± 0.0007	0.14 ± 0.01	< 0	0.152 ± 0.002	0.0027 ± 0.0005
GX 354 - 0	NS	262.99	-33.83	8.1 ± 0.07	10.97 ± 0.08	5.82 ± 0.1	0.54 ± 0.02	0.25 ± 0.01	1.23 ± 0.06	0.298 ± 0.006	0.027 ± 0.001
1H 1746 - 370	-	267.55	-37.05	1.61 ± 0.02	< 0.1	< 0.4	0.58 ± 0.05	1 ± 3	147 ± 159	0.14 ± 0.02	< 0.046
H 1755 - 338	BH	269.67	-33.81	1.0 ± 0.03	< -1.11	< 0.2	14.2 ± 0.5	< 0	< 0	< 1.4	< 0.45
GX 5 - 1	NS	270.28	-25.08	129.2 ± 0.1	74.5 ± 0.1	3.5 ± 0.2	0.0314 ± 0.0007	0.121 ± 0.002	0.43 ± 0.1	0.1757 ± 0.0006	0.0021 ± 0.0001
GX 9 + 1	NS	270.39	-20.53	76.8 ± 0.1	51.1 ± 0.1	1.6 ± 0.1	0.031 ± 0.001	0.074 ± 0.002	0.0 ± 0.2	0.216 ± 0.001	0.0013 ± 0.0002
GX 13 + 1	NS	273.63	-17.16	37.8 ± 0.1	16.22 ± 0.08	< 0.9	0.067 ± 0.003	0.263 ± 0.009	< 0	0.156 ± 0.002	< 0.005
GX 17 + 2	NS	274.01	-14.04	77.78 ± 0.08	59.0 ± 0.1	3.8 ± 0.1	0.0145 ± 0.0004	0.106 ± 0.002	0.43 ± 0.06	0.2379 ± 0.0006	0.0029 ± 0.0001
H 1820 - 303	NS	275.92	-30.36	37.33 ± 0.05	28.4 ± 0.1	2.2 ± 0.1	0.049 ± 0.001	0.134 ± 0.005	0.3 ± 0.1	0.26 ± 0.001	0.003 ± 0.0002
GS 1826 - 24	NS	277.37	-23.80	29.15 ± 0.05	7.9 ± 0.1	< 0.8	0.037 ± 0.001	0.48 ± 0.03	< 0	0.099 ± 0.001	< 0.0037
4U 1722 - 30	NS	261.89	-30.80	1.12 ± 0.03	0.72 ± 0.08	0.9 ± 0.1	5.0 ± 0.2	5.2 ± 0.9	0.5 ± 0.4	0.17 ± 0.01	0.018 ± 0.004
Swift J174510.8 - 2624	-	266.30	-26.40	6.4 ± 0.3	5.2 ± 0.1	< 0.09	3.3 ± 0.3	1.01 ± 0.06	< 0	0.16 ± 0.02	< 0.05
1A 1744 - 361	NS	267.08	-36.12	0.18 ± 0.03	< -0.35	< 0.31	10 ± 3	0.7 ± 0.6	< 0	< 1.2	< 1.1
GRS 1758 - 258	BH	270.30	-25.74	3.4 ± 0.1	2.7 ± 0.1	8.9 ± 0.2	40.3 ± 0.7	10.8 ± 0.5	0.31 ± 0.03	0.049 ± 0.01	0.037 ± 0.005
SAX J1806.5 - 2215	NS	271.63	-22.24	0.36 ± 0.06	< 0.7	< 0.0	7 ± 2	0 ± 37	< 0	< 0.45	< 0.06
XTE J1806 - 246	NS	271.71	-24.58	1.21 ± 0.05	< -1.0	< -0.2	13.5 ± 0.5	1.3 ± 0.4	< 0	< 0.62	< 0.042
4U 1812 - 12	NS	273.78	-12.10	1.06 ± 0.03	0.79 ± 0.07	2.0 ± 0.1	0.6 ± 0.1	0.3 ± 0.5	0.15 ± 0.1	0.24 ± 0.03	0.067 ± 0.007
3A 1850 - 087	-	283.27	-8.71	0.6 ± 0.02	< -0.11	< 0.9	1.0 ± 0.2	< 0	1 ± 2	< 0.58	< 0.1
4U 1916 - 053	NS	289.70	-5.24	0.65 ± 0.02	< 0.5	1.1 ± 0.2	0.7 ± 0.1	< 0	< 0	< 0.64	0.08 ± 0.01
SAX J1828.5 - 1037	NS	277.14	-10.62	0.39 ± 0.03	< 0.41	< 0.2	1.5 ± 0.5	< 0	< 0	< 0.75	< 0.28
Ser X - 1	NS	279.99	5.04	32.16 ± 0.05	13.6 ± 0.1	0.7 ± 0.1	0.0156 ± 0.0007	0.19 ± 0.01	< 0	0.14 ± 0.001	0.0016 ± 0.0002
4U 1957 + 115	BH	299.85	11.71	7.24 ± 0.05	1.1 ± 0.2	< 3.1	0.078 ± 0.007	70 ± 4	< 0	0.065 ± 0.008	< 0.057
4U 1543 - 624	NScandidate	236.98	-62.57	1.22 ± 0.05	< 0.0	< 1.3	1.5 ± 0.2	< 0	12 ± 8	< 0.46	< 0.14
H 1608 - 522	NS	243.18	-52.42	2.11 ± 0.03	0.77 ± 0.08	1.7 ± 0.1	33.2 ± 0.5	201 ± 5	8.0 ± 0.7	0.115 ± 0.006	< 0.011
H 1636 - 536	NS	250.23	-53.75	4.62 ± 0.03	4.4 ± 0.09	7.7 ± 0.1	0.39 ± 0.02	0.34 ± 0.03	0.47 ± 0.03	0.27 ± 0.007	0.046 ± 0.001
GX 340 + 0	NS	251.45	-45.61	45.3 ± 0.2	37.0 ± 0.1	1.8 ± 0.1	0.055 ± 0.003	0.155 ± 0.004	0.6 ± 0.2	0.262 ± 0.002	0.0031 ± 0.0004
1H 1556 - 605	-	240.26	-60.74	0.78 ± 0.05	< 0.12	< 1.2	0.4 ± 0.2	< 0	< 0	< 0.45	< 0.08
H 1624 - 490	NS	247.01	-49.20	3.91 ± 0.06	4.18 ± 0.09	< 0.6	0.45 ± 0.04	0.37 ± 0.04	< 0	0.24 ± 0.01	< 0.026
IGR J16287 - 5021	-	247.11	-50.38	0.19 ± 0.03	< 0.01	< 0.09	16 ± 3	4 ± 2	< 0	< 0.8	< 0.17
H 1705 - 440	NS	257.23	-44.10	21.21 ± 0.07	15.75 ± 0.1	< 0.6	0.605 ± 0.01	0.48 ± 0.01	63 ± 56	0.207 ± 0.002	< 0.0036
4U 1735 - 444	NS	264.74	-44.45	16.9 ± 0.05	12.9 ± 0.1	1.2 ± 0.1	0.094 ± 0.003	0.16 ± 0.01	< 0	0.219 ± 0.003	0.0029 ± 0.0005

Table 8 continued



Table 8 (continued)

Source name	Compact object	R.A.	Dec.	$R_{2-6\text{ keV}}$	$R_{7-40\text{ keV}}$	$R_{25-100\text{ keV}}$	$F_{\text{rms}}1^c$	$F_{\text{rms}}2^d$	$F_{\text{rms}}3^e$	HRI <sup>a</sup>	HR2 <sup>b</sup>
(1)	(2)	(deg)	(deg)	cts s <sup>-1</sup>	cts s <sup>-1</sup>	cts s <sup>-1</sup>	(8)	(9)	(10)	(11)	(12)
XTE J1701 – 407	NS	255.43	-40.86	0.73 ± 0.05	0.42 ± 0.08	< 0.3	2.9 ± 0.4	36 ± 4	6 ± 7	< 0.41	< 2.4
H 1702 – 429	NS	256.56	-43.04	5.77 ± 0.07	4.01 ± 0.1	4.1 ± 0.1	0.95 ± 0.04	0.36 ± 0.05	1.01 ± 0.07	0.161 ± 0.008	0.048 ± 0.003
4U 1708 – 40	NS	258.10	-40.84	1.41 ± 0.05	< 0.63	< -0.6	1.2 ± 0.1	383 ± 21	< 0	0.12 ± 0.02	< 0.048
3A 1822 – 371	NS	276.45	-37.10	1.44 ± 0.03	2.8 ± 0.1	3.4 ± 0.2	0.2 ± 0.04	0.9 ± 0.1	0.03 ± 0.05	0.48 ± 0.03	0.093 ± 0.007
H 1822 – 000	–	276.34	-0.01	2.16 ± 0.02	< 0.5	< 0.4	0.16 ± 0.02	< 0	106 ± 146	< 0.19	< 0.063
Aql X – 1	NS	287.82	0.58	0.65 ± 0.02	< 0.21	< 0.8	505 ± 3	468 ± 26	17 ± 5	0.11 ± 0.003	< 0.0031
MAXI J1820 + 070	BH	275.09	7.19	4.09 ± 0.04	6.9 ± 0.2	< 2.5	961 ± 2	121 ± 1	17779 ± 220	0.041 ± 0.001	0.25 ± 0.01
4U 1323 – 62	NS	201.65	-62.14	0.36 ± 0.03	< 0.41	1.3 ± 0.2	< 0	1364 ± 4793	0.5 ± 0.3	< 0.7	< 0.27
4U 1918 + 146	–	290.07	14.70	0.22 ± 0.03	< -0.4	< 0.4	< 0	< 0	< 0	< 2.0	< 0.6
Cyg X – 2	NS	326.17	38.32	68.0 ± 0.2	30.0 ± 0.5	< 4.7	0.153 ± 0.004	0.1 ± 0.02	0.3 ± 0.7	0.128 ± 0.003	< 0.0067
IGR J00291 + 5934	NS	7.26	59.57	0.16 ± 0.03	< -0.1	< 0.8	< 0	< 0	< 0	< 4.8	< 0.47
H 0614 + 091	NS	94.28	9.14	6.33 ± 0.04	1.6 ± 0.2	2.3 ± 0.2	0.23 ± 0.01	0.5 ± 0.3	0.1 ± 0.1	0.083 ± 0.008	0.017 ± 0.002
3A 0921 – 630	–	140.65	-63.29	0.27 ± 0.04	< 0.6	< 1.6	< 0	< 0	< 0	< 1.2	< 0.3
1H 1254 – 690	NS	194.40	-69.29	3.72 ± 0.05	0.6 ± 0.1	< 1.7	0.03 ± 0.01	2 ± 1	47 ± 38	0.12 ± 0.02	< 0.064
3A 1246 – 588	NS	192.41	-59.09	0.29 ± 0.03	< -0.34	< 0.5	0.7 ± 0.6	< 0	< 0	< 0.7	< 0.07
1E 1740.7 – 2942	BH	265.98	-29.75	< 0.29	7.9 ± 0.1	12.1 ± 0.2	278 ± 32	0.49 ± 0.03	0.16 ± 0.02	0.32 ± 0.05	0.23 ± 0.04
GRO J1744 – 28	NS	266.14	-28.74	< 0.12	4.8 ± 0.1	3.7 ± 0.2	< 0	2.1 ± 0.1	0.25 ± 0.07	< 160	< 70
SLX 1744 – 300	NS	266.86	-30.05	< 1.4	3.2 ± 0.1	1.4 ± 0.1	69 ± 10	4.4 ± 0.2	0.8 ± 0.3	< 1.0	< 40
IGR J17497 – 2821	BH	267.41	-28.35	< 0.13	0.86 ± 0.09	< 0.7	< 0	13 ± 1	< 0	< 0.53	< 3.3
SAX J1750.8 – 2900	NS	267.60	-29.04	< 0.11	0.59 ± 0.09	< 0.8	< 0	29 ± 3	1 ± 6	< 20	< 0.13
IGR J17473 – 2721	NS	266.83	-27.34	< 0.5	0.9 ± 0.1	< 0.8	< 0	93 ± 4	18 ± 6	< 0.7	–
SLX 1735 – 269	NS	264.57	-26.99	< 0.53	< 0.32	0.7 ± 0.1	11 ± 3	409 ± 115	0.8 ± 0.7	< 0.9	< 0.2
H 0918 – 549	NS	140.11	-55.21	< 0.22	< 0.1	0.8 ± 0.1	< 0	< 0	< 0	< 3.8	< 0.35
MAXI J1348 – 630	BH	207.05	-63.27	1.1 ± 0.03	0.46 ± 0.09	12.3 ± 0.2	4441 ± 8	5618 ± 45	90.2 ± 0.5	0.0413 ± 0.0007	0.267 ± 0.003

NOTE—

<sup>a</sup> and <sup>b</sup> are HR (7–40 keV, 2–6 keV) and HR (25–100 keV, 2–6 keV) calculated with Equation 7, respectively.<sup>c–e</sup> Excess variances calculated with Equation 5 at 2–6 keV, 7–40 keV and 25–100 keV, respectively.

Table 9. The First Four-year GPSS Catalog of *Insight-HXMT* (High Mass X-ray Binary).

Source name	Compact object	R.A. (deg)	Dec. (deg)	$R_{2-6\text{ keV}}$ cts s $^{-1}$	$R_{7-40\text{ keV}}$ cts s $^{-1}$	$R_{25-100\text{ keV}}$ cts s $^{-1}$	$F_{\text{rms}1^c}$	$F_{\text{rms}2^d}$	$F_{\text{rms}3^e}$	HR1 $^e$	HR2 $^b$
(1)	(2)	(3)	(4)	(5)	(6)	(7)	(8)	(9)	(10)	(11)	(12)
IGR J17252 – 3616	NS	261.30	–36.28	0.17 ± 0.03	< 0.27	< 0.7	10 ± 3	582 ± 158	2 ± 5	< 0.8	< 0.11
GRO J1750 – 27	NS	267.30	–26.65	5.4 ± 0.2	12.08 ± 0.09	< 0.03	9.4 ± 0.5	0.4 ± 0.01	< 0	0.065 ± 0.008	–
<b>4U1700 – 377</b>	NS	255.99	–37.84	1.29 ± 0.04	9.49 ± 0.1	19.6 ± 0.2	15.4 ± 0.5	9.1 ± 0.1	2.4 ± 0.04	0.67 ± 0.02	0.175 ± 0.007
IGR J17586 – 2129	–	269.64	–21.39	0.38 ± 0.05	< –0.1	< 0.3	161 ± 6	< 0	< 0	< 0.45	< 0.034
SAX J1818.6 – 1703	NS	274.66	–17.05	0.68 ± 0.06	< 0.3	< 0.6	23 ± 1	< 0	< 0	< 0.26	< 0.057
AX J1820.5 – 1434	–	275.12	–14.57	0.5 ± 0.06	0.5 ± 0.1	< 0.6	23 ± 2	2 ± 1	< 0	< 0.14	< 0.036
IGR J18256 – 1035	–	276.43	–10.58	0.32 ± 0.03	< 0.18	< 0.5	2.5 ± 0.7	< 0	< 0	< 0.8	< 0.19
AX 1845.0 – 0433	NS	281.92	–4.50	0.26 ± 0.02	< –0.08	< 0.2	0.7 ± 0.7	< 0	< 0	< 0.7	< 0.11
IGR J18483 – 0311	NS	282.07	–3.17	0.4 ± 0.04	< 0.61	2.1 ± 0.1	< 0	159 ± 16	18.8 ± 0.9	< 0.8	< 0.6
NS	NS	283.88	–2.61	0.27 ± 0.02	< 0.45	0.7 ± 0.1	0.3 ± 0.4	773 ± 372	4 ± 1	< 1.0	0.09 ± 0.02
NS	–	284.50	–2.70	0.16 ± 0.02	< 0.09	< 0.4	< 0	6 ± 3	< 0	< 1.4	< 0.44
GS 1855 – 02	NS	284.50	–2.70	0.16 ± 0.02	< 0.09	< 0.4	< 0	6 ± 3	< 0	< 0.59	< 0.32
IGR J18450 – 0435	NS	281.26	–4.57	0.36 ± 0.03	< 0.15	< 0.3	0.3 ± 0.3	< 0	< 0	< 2.0	< 0.6
XTE J1858 + 034	NS	284.68	3.44	0.17 ± 0.03	< –0.2	< 0.2	< 0	< 0	0 ± 3	< 0.68 ± 0.03	0.041 ± 0.003
4U 1901 + 03	NS	285.90	3.19	0.31 ± 0.02	< 1.0	< 0.8	14 ± 1	65 ± 4	15 ± 6	0.68 ± 0.03	0.3 ± 0.02
<b>H 1417 – 624</b>	NS	215.30	–62.70	0.98 ± 0.03	2.22 ± 0.09	2.4 ± 0.2	1.0 ± 0.1	4.6 ± 0.3	15.8 ± 0.8	1.2 ± 0.05	0.3 ± 0.02
Cir X – 1	–	230.17	–57.17	12.11 ± 0.04	10.62 ± 0.09	< 1.0	5.32 ± 0.03	1.19 ± 0.03	< 0	0.136 ± 0.001	< 0.0023
H 1553 – 542	NS	239.45	–54.42	0.16 ± 0.03	< 0.3	< 0.4	2 ± 2	1850 ± 169	< 0	0.6 ± 0.1	< 0.34
GX 339 – 4	BH	255.71	–48.79	1.74 ± 0.03	< 0.24	1.2 ± 0.1	144 ± 1	2004 ± 76	18 ± 1	0.46 ± 0.01	< 0.0045
IGR J16207 – 5129	NS	245.19	–51.50	0.15 ± 0.03	< –0.12	< 0.2	43 ± 5	0 ± 1	< 0	< 0.74	< 0.12
<b>IGR J16318 – 4848</b>	NS	247.95	–48.82	1.07 ± 0.09	1.06 ± 0.09	1.2 ± 0.1	4.5 ± 0.6	1.6 ± 0.5	3.3 ± 0.6	< 0.42	< 0.14
IGR J16327 – 4940	–	248.17	–49.70	0.24 ± 0.04	< 0.28	< 0.1	23 ± 3	51 ± 20	< 0	< 0.28	< 0.18
IGR J16418 – 4532	NS	250.46	–45.54	2.6 ± 0.2	< 0.3	< 0.9	4.9 ± 0.4	< 0	6 ± 3	< 0.28	< 0.049
SCT X – 1	NS	279.12	–7.61	0.11 ± 0.02	< 0.15	< 0.3	< 0	< 0	< 0	< 2.6	< 0.28
IGR J18410 – 0535	NS	280.25	–5.60	0.3 ± 0.04	< 0.27	< 0.5	2.6 ± 0.8	< 0	< 0	< 0.51	< 0.11
<b>H 1538 – 522</b>	NS	235.60	–52.39	0.68 ± 0.03	1.9 ± 0.09	1.5 ± 0.1	1.0 ± 0.2	4.9 ± 0.3	0.7 ± 0.3	0.75 ± 0.05	0.068 ± 0.008
4U 1543 – 47	BH	236.79	–47.67	0.29 ± 0.02	< –0.51	< 0.4	139261 ± 167	2.9 ± 0.6	< 0	0.0042 ± 0.0005	< 0.0005
SS 433	–	287.96	4.98	0.77 ± 0.03	< 0.6	1.4 ± 0.2	< 0	100 ± 254	0.2 ± 0.3	< 0.52	0.11 ± 0.01
XTE J1908 + 094	BH	287.22	9.39	0.35 ± 0.06	< 1.0	< 1.4	0.3 ± 0.7	0 ± 1	0 ± 3	< 5.3	< 0.6
4U 1909 + 07	NS	287.70	7.60	0.26 ± 0.03	0.76 ± 0.1	< 1.4	< 0	1.1 ± 0.8	4 ± 4	< 1.5	< 0.29
<b>IGR J19140 + 0951</b>	NS	288.52	9.88	0.33 ± 0.04	0.9 ± 0.1	1.3 ± 0.2	0.8 ± 0.8	1.4 ± 0.7	20 ± 2	< 0.7	< 0.19
<b>Cen X – 3</b>	NS	170.32	–60.62	2.58 ± 0.03	10.12 ± 0.09	5.1 ± 0.1	10.6 ± 0.2	4.05 ± 0.07	1.06 ± 0.08	0.782 ± 0.008	0.0375 ± 0.0009
IGR J11435 – 6109	NS	176.00	–61.13	0.17 ± 0.03	< 0.04	< 0.4	< 0	< 0	31 ± 20	< 0.59	< 0.42
NS	NS	186.66	–62.77	1.19 ± 0.03	6.8 ± 0.1	19.0 ± 0.2	1.5 ± 0.1	31.8 ± 0.5	2.74 ± 0.08	1.53 ± 0.08	0.53 ± 0.02
<b>GX 301 – 2</b>	NS	195.32	–61.60	0.16 ± 0.03	< –0.51	< 0.2	2 ± 1	0.8 ± 0.4	2 ± 2	< 3.8	< 1.1
GX 304 – 1	NS	176.87	–61.95	0.38 ± 0.04	< 0.78	1.4 ± 0.1	0.6 ± 0.4	15 ± 7	3.2 ± 0.5	0.49 ± 0.09	0.18 ± 0.03
1E 1145.1 – 6141	NS	176.87	–61.95	0.38 ± 0.04	< 0.78	1.4 ± 0.1	0.6 ± 0.4	15 ± 7	3.2 ± 0.5	0.49 ± 0.09	0.18 ± 0.03

Table 9 continued

Table 9 (continued)

Source name	Compact object	R.A.	Dec.	$R_{2-6\text{ keV}}$	$R_{7-40\text{ keV}}$	$R_{25-100\text{ keV}}$	$F_{\text{rms}} 1^c$	$F_{\text{rms}} 2^d$	$F_{\text{rms}} 3^e$	HR1 <sup>a</sup>	HR2 <sup>b</sup>
(1)	(2)	(deg)	(deg)	cts s <sup>-1</sup>	cts s <sup>-1</sup>	cts s <sup>-1</sup>	(8)	(9)	(10)	(11)	(12)
PSR B1259 - 63	NS	195.75	-63.83	0.23 ± 0.03	< -0.54	< 0.3	< 0	0.1 ± 0.3	0 ± 6	< 1.9	< 0.2
4U1210 - 64	NS	183.45	-64.84	0.31 ± 0.04	< -0.6	< 0.6	2.7 ± 1.0	< 0	< 0	< 0.59	< 0.06
IGR J19294 + 1816	NS	292.48	18.31	0.51 ± 0.03	< 0.6	3.0 ± 0.2	0.6 ± 0.2	1859 ± 277	1.5 ± 0.2	0.71 ± 0.09	0.13 ± 0.02
XTE J1946 + 274	NS	296.41	27.36	0.24 ± 0.02	< -0.2	< 0.7	3.6 ± 0.7	18 ± 2	< 0	1.34 ± 0.09	< 0.31
3A 1954 + 319	NS	298.93	32.10	0.15 ± 0.02	< 0.1	< 1.1	12 ± 2	1 ± 1	5 ± 2	0.8 ± 0.1	0.11 ± 0.01
EXO 2030 + 375	NS	308.06	37.64	0.28 ± 0.02	< 0.7	1.8 ± 0.1	14 ± 1	192 ± 24	8.1 ± 0.7	0.63 ± 0.05	0.16 ± 0.01
<b>Cyg X - 3</b>	NS	308.11	40.96	13.1 ± 0.05	19.1 ± 0.1	14.9 ± 0.2	2.22 ± 0.02	0.42 ± 0.01	0.42 ± 0.02	0.156 ± 0.002	0.009 ± 0.0003
SAX J2103.5 + 4545	NS	315.90	45.75	0.28 ± 0.02	< 0.1	< 1.1	1.0 ± 0.5	< 0	0.7 ± 0.9	< 0.7	< 0.13
3A 2206 + 543	NS	331.98	54.52	0.12 ± 0.02	< -0.28	< 1.2	< 0	< 0	< 0	< 1.5	< 0.25
IGR J22534 + 6243	NS	343.48	62.73	0.14 ± 0.02	< -0.1	< 0.7	< 0	< 0	< 0	< 5.1	< 0.18
<b>GRS 1915 + 105</b>	BH	288.80	10.95	1.97 ± 0.05	7.9 ± 0.1	11.7 ± 0.2	759 ± 3	59.4 ± 0.5	0.79 ± 0.06	0.201 ± 0.003	0.0012 ± 0.0002
<b>Cyg X - 1</b>	BH	299.59	35.20	121.53 ± 0.09	33.0 ± 0.1	70.1 ± 0.2	0.1269 ± 0.0009	1.31 ± 0.02	0.811 ± 0.01	0.0717 ± 0.0004	0.0186 ± 9e - 05
3A 0114 + 650	NS	19.51	65.29	0.26 ± 0.02	< 0.4	0.7 ± 0.1	1.4 ± 0.5	23 ± 27	1.9 ± 0.9	< 0.79	< 0.28
RX J0146.9 + 6121	NS	26.75	61.36	0.24 ± 0.02	< 0.18	< 1.1	2.2 ± 0.7	< 0	< 0	< 0.7	< 0.07
<b>1A 0535 + 262</b>	NS	84.73	26.32	0.75 ± 0.03	2.9 ± 0.1	5.3 ± 0.2	197 ± 2	394 ± 4	70.2 ± 0.7	1.34 ± 0.02	0.299 ± 0.004
<b>Vela X - 1</b>	NS	135.53	-40.56	2.56 ± 0.03	12.4 ± 0.2	32.2 ± 0.2	3.26 ± 0.1	3.2 ± 0.1	1.1 ± 0.02	1.12 ± 0.02	0.216 ± 0.003
IGR J08408 - 4503	NS	130.20	-45.06	0.19 ± 0.04	< 0.0	< 1.2	1 ± 1	< 0	1 ± 13	< 0.7	< 0.17
<b>GRO J1008 - 57</b>	NS	152.44	-58.29	0.44 ± 0.02	0.94 ± 0.09	4.4 ± 0.1	14.6 ± 0.8	29 ± 1	3.5 ± 0.1	0.57 ± 0.04	0.14 ± 0.005
OAO 1657 - 415	NS	255.20	-41.66	< 0.41	3.9 ± 0.08	7.5 ± 0.1	112 ± 13	2.8 ± 0.1	1.25 ± 0.05	0.83 ± 0.1	0.28 ± 0.04
IGR J16320 - 4751	NS	248.01	-47.87	< 0.28	1.11 ± 0.07	1.7 ± 0.1	109 ± 38	15.4 ± 0.9	1.1 ± 0.3	< 0.64	< 0.33
<b>Swift J0243.6 + 6124</b>	NS	40.92	61.43	0.82 ± 0.02	5.89 ± 0.09	29.5 ± 0.1	5186 ± 10	774 ± 2	66.6 ± 0.2	0.466 ± 0.003	0.0758 ± 0.0003

NOTE—

<sup>a</sup> and <sup>b</sup> are HR (7-40 keV, 2-6 keV) and HR (25-100 keV, 2-6 keV) calculated with Equation 7, respectively.<sup>c,e</sup> Excess variances calculated with Equation 5 at 2-6 keV, 7-40 keV and 25-100 keV, respectively.

**Table 10.** The First Four-year GPSS Catalog of *Insight-HXMT* (SNR).

Source name	R.A. (deg)	Dec. (deg)	$R_{2-6\text{ keV}}$ cts s <sup>-1</sup>	$R_{7-40\text{ keV}}$ cts s <sup>-1</sup>	$R_{25-100\text{ keV}}$ cts s <sup>-1</sup>	$F_{\text{rms}1^c}$	$F_{\text{rms}2^d}$	$F_{\text{rms}3^e}$	HR1 <sup>a</sup>	HR2 <sup>b</sup>
(1)	(2)	(3)	(4)	(5)	(6)	(7)	(8)	(9)	(10)	(11)
RX J1713.7 – 3946	258.39	-39.76	1.12 ± 0.05	< 0.87	< 0.0	2.8 ± 0.3	12 ± 3	5 ± 5	< 0.19	< 0.078
IGR J18135 – 1751	273.40	-17.83	0.5 ± 0.1	0.69 ± 0.08	< 0.8	65 ± 4	10 ± 1	< 0	< 0.14	< 0.5
SNR 021.5 – 00.9	278.40	-10.56	0.24 ± 0.03	< 0.44	< 0.6	0.1 ± 0.8	< 0	< 0	< 0.59	< 0.2
AX J1850.2 – 0025	282.56	-0.42	0.18 ± 0.03	< -0.02	< 0.5	< 0	< 0	< 0	< 2.2	< 0.26
HESS J1834 – 087	278.73	-8.73	0.16 ± 0.03	< 0.27	< 0.3	< 0	< 0	< 0	< 0.66	< 0.29
AX J1838.0 – 0655	279.51	-6.90	0.44 ± 0.03	< 0.08	< 0.4	0.2 ± 0.3	< 0	< 0	< 0.44	< 0.13
SN 1006	225.70	-41.91	0.28 ± 0.06	< 0.9	< 3.5	< 0	< 0	< 0	< 2.5	< 1.6
0FGL J1923.0 + 1411	290.83	14.16	0.25 ± 0.03	< -0.7	< 0.4	< 0	< 0	< 0	< 2.8	< 0.44
SNR 074.0 – 08.5	313.06	31.28	0.21 ± 0.04	< 0.3	< 1.6	< 0	< 0	< 0	< 2.2	< 0.6
Cas A	350.87	58.81	8.74 ± 0.03	< 0.8	< 1.1	< 0	< 0	< 0	0.028 ± 0.005	0.0054 ± 0.001
Crab	83.63	22.01	134.0 ± 0.1	135.5 ± 0.2	180.5 ± 0.2	0.00083 ± 8e - 05	0.0002 ± 0.0002	< 0	0.3193 ± 0.0007	0.072 ± 0.0001
SNR 189.1 + 03.0	94.51	22.66	0.3 ± 0.02	< -0.3	< 0.6	0.2 ± 0.2	0.1 ± 0.5	< 0	< 1.9	< 0.15
SNR 260.4 – 03.4	126.03	-43.00	1.39 ± 0.04	< 0.2	< 1.2	0.11 ± 0.07	< 0	< 0	< 0.6	< 0.11

NOTE—

<sup>a</sup> and <sup>b</sup> are HR (7–40 keV, 2–6 keV) and HR (25–100 keV, 2–6 keV) calculated with Equation 7, respectively.<sup>c, e</sup> Excess variances calculated with Equation 5 at 2–6 keV, 7–40 keV and 25–100 keV, respectively.

**Table 11.** The First Four-year GPSS Catalog of *Insight-HXMT* (Pulsar).

Source name	R.A. (deg)	Dec. (deg)	$R_{2-6 \text{ keV}}$ cts s <sup>-1</sup>	$R_{7-40 \text{ keV}}$ cts s <sup>-1</sup>	$R_{25-100 \text{ keV}}$ cts s <sup>-1</sup>	$F_{\text{rms}1^c}$	$F_{\text{rms}2^d}$	$F_{\text{rms}3^e}$	HR1 <sup>a</sup>	HR2 <sup>b</sup>
(1)	(2)	(3)	(4)	(5)	(6)	(7)	(8)	(9)	(10)	(11)
PSR B1509 – 58	228.48	-59.14	0.47 ± 0.05	< 0.54	1.4 ± 0.2	< 0	96 ± 85	< 0	< 0.7	< 0.17
2EGS J1418 – 6049	215.00	-60.60	0.15 ± 0.03	< -0.24	< 0.5	< 0	103 ± 4	< 0	< 3.5	< 1.7
MAXI J1409 – 619	212.01	-61.98	0.18 ± 0.03	< -0.58	< 0.5	< 0	0.1 ± 0.3	< 0	< 2.5	< 0.4
HESS J1614 – 518	243.62	-51.82	0.55 ± 0.03	< 0.08	< 0.4	12.4 ± 0.8	5 ± 2	< 0	< 0.3	< 0.07
PSR J1617 – 5055	244.37	-50.92	0.19 ± 0.04	< 0.15	< 0.3	13 ± 3	10 ± 7	< 0	< 0.77	< 0.11
IGR J17088 – 4008	257.21	-40.14	0.76 ± 0.05	< 0.59	< 0.0	4.0 ± 0.5	111 ± 14	12 ± 2	< 0.24	< 0.03
GEV J1837 – 0610	279.25	-6.17	0.11 ± 0.02	< 0.09	< 0.4	< 0	< 0	< 0	< 0.7	< 0.24
GEV J1907 + 0557	286.92	5.95	0.18 ± 0.03	< 0.0	< 0.6	2 ± 1	< 0	< 0	< 1.5	< 0.18
3EG J1928 + 1733	292.00	17.60	0.21 ± 0.03	< -0.17	< 0.7	3 ± 1	< 0	< 0	< 1.7	< 0.47
0FGL J1954.4 + 2838	298.58	28.60	0.13 ± 0.03	< -0.6	< 0.3	< 0	< 0	< 0	< 3.1	< 0.32
Vela Pulsar	128.84	-45.18	1.88 ± 0.04	< 0.8	1.2 ± 0.2	0.13 ± 0.03	< 0	< 0	–	0.031 ± 0.005

NOTE—

<sup>a</sup> and <sup>b</sup> are HR (7–40 keV, 2–6 keV) and HR (25–100 keV, 2–6 keV) calculated with Equation 7, respectively.<sup>c–e</sup> Excess variances calculated with Equation 5 at 2–6 keV, 7–40 keV and 25–100 keV, respectively.

**Table 12.** The First Four-year GPSS Catalog of *Insight-HXMT* (Seyfert 1 Galaxy).

Source name	R.A.	Dec.	$R_{2-6\text{ keV}}$	$R_{7-40\text{ keV}}$	$R_{25-100\text{ keV}}$	$F_{\text{rms}1}^c$	$F_{\text{rms}2}^d$	$F_{\text{rms}3}^e$	HR1 <sup>a</sup>	HR2 <sup>b</sup>
(1)	(deg)	(deg)	cts s <sup>-1</sup>	cts s <sup>-1</sup>	cts s <sup>-1</sup>	(7)	(8)	(9)	(10)	(11)
IGR.J18259-0706	276.49	-7.17	0.21 ± 0.02	< -0.43	< 0.5	1.9 ± 1.2	< 0	< 0	< 2.0	< 0.21
IGR.J18538-0102	283.45	-1.04	0.29 ± 0.02	< -0.1	< 0.3	< 0	4 ± 1	< 0	< 0.7	< 0.27
IGR.J16119-6036	242.96	-60.63	1.15 ± 0.04	< 0.05	< 1.2	0.28 ± 0.08	< 0	< 0	< 0.3	< 0.07
4U 1344-60	206.90	-60.62	0.17 ± 0.03	< -0.42	< 1.7	0 ± 1	1.4 ± 0.6	< 0	< 1.3	< 0.58
IGR.J16056-6110	241.46	-61.20	0.81 ± 0.09	< 0.1	< 1.1	0.0 ± 0.2	< 0	< 0	< 0.5	< 0.22
IGR.J21247+5058	321.16	50.97	0.28 ± 0.02	< 0.2	1.1 ± 0.1	< 0	< 0	< 0	< 1.9	< 0.26

NOTE—

<sup>a</sup> and <sup>b</sup> are HR (7–40 keV, 2–6 keV) and HR (25–100 keV, 2–6 keV) calculated with Equation 7, respectively.<sup>c, e</sup> Excess variances calculated with Equation 5 at 2–6 keV, 7–40 keV and 25–100 keV, respectively.



Table 13. The First Four-year GPSS Catalog of *Insight-HXMT* (Unclassified and others).

Source name	Source type*	R.A.	Dec.	$R_{2-6\text{ keV}}$	$R_{7-40\text{ keV}}$	$R_{25-100\text{ keV}}$	$F_{\text{rms}}1^c$	$F_{\text{rms}}2^d$	$F_{\text{rms}}3^e$	HRI <sup>a</sup>	HR2 <sup>b</sup>
(1)	(2)	(deg) (3)	(deg) (4)	cts s <sup>-1</sup> (5)	cts s <sup>-1</sup> (6)	cts s <sup>-1</sup> (7)	(8)	(9)	(10)	(11)	(12)
IGR J17385 - 3433	Unclassified	264.63	-34.55	0.23 ± 0.03	< -0.33	< 0.56	5 ± 1	1.6 ± 0.5	< 0	< 0.9	< 0.062
4PBC J1709.7 - 2348	Unclassified	257.45	-23.75	0.38 ± 0.05	< 0.9	< 1.4	2.2 ± 0.8	4 ± 2	< 0	< 0.54	< 0.20
IGR J17239 - 3143	Unclassified	260.97	-31.72	0.26 ± 0.03	< 0.03	< 0.34	2 ± 1	20 ± 3	< 0	< 0.5	< 0.13
HESS J1804 - 216	Unclassified	271.17	-21.68	1.05 ± 0.06	< 0.32	< 0.4	9.2 ± 0.6	< 0	< 0	< 0.07	< 0.014
IGR J18172 - 1944	Unclassified	274.31	-19.74	0.53 ± 0.03	< -0.41	< 0.29	4.4 ± 0.5	0.8 ± 0.5	< 0	< 0.27	< 0.057
Swift J1728.9 - 3613	Unclassified	262.24	-36.23	0.48 ± 0.03	< 0.23	< 1.0	25 ± 1	30 ± 19	4 ± 1	< 0.09	< 0.02
Swift J1729.9 - 3437	Unclassified	262.54	-34.61	0.89 ± 0.06	< 0.9	< 0.56	4.7 ± 0.5	39 ± 11	< 0	< 0.23	< 0.06
AX J1825.5 - 1144	Unclassified	276.38	-11.75	0.14 ± 0.02	< 0.07	< 0.24	0 ± 2	< 0	< 0	< 0.7	< 0.11
AX J1828.7 - 1116	Unclassified	277.20	-11.28	0.16 ± 0.03	< 0.21	< 0.1	0 ± 1	< 0	< 0	< 0.7	< 0.24
AX J1848.8 - 0129	Unclassified	282.20	-1.49	0.19 ± 0.03	< 0.07	< 0.3	< 0	< 0	< 0	< 1.3	< 2.1
AX J1852.6 + 0038	Unclassified	283.17	0.65	0.28 ± 0.02	< -0.37	< 0.3	< 0	< 0	< 0	< 0.8	< 0.2
AX J1855.8 + 0129	Unclassified	283.97	1.49	0.49 ± 0.03	< -0.32	< 0.1	0.4 ± 0.2	2.4 ± 0.7	< 0	< 2.6	< 0.12
XTE J1901 + 014	Unclassified	285.42	1.44	0.29 ± 0.02	< -0.42	< 0.5	0.5 ± 0.5	< 0	< 0	< 0.8	< 0.18
AX J1841.3 - 0455	Unclassified	280.33	-4.94	0.37 ± 0.04	< 0.41	< 0.5	0.1 ± 0.4	< 0	< 0	< 1.3	< 0.11
GRO J1838 - 04	Unclassified	279.38	-4.53	0.31 ± 0.02	< -0.07	< 0.3	1.1 ± 0.4	< 0	< 0	< 0.6	< 0.21
2EGS J1903 + 0529	Unclassified	286.00	5.80	0.18 ± 0.02	< -0.33	< 0.1	< 0	0.2 ± 0.5	< 0	< 2.5	< 0.7
AX J1905.5 + 0659	Unclassified	286.40	6.98	0.12 ± 0.02	< -0.18	< 0.5	4 ± 3	0.8 ± 0.9	0 ± 1	< 4.6	< 1.2
Swift J1845.7 - 0087	Unclassified	281.48	-0.66	0.2 ± 0.02	< -0.03	< 0.7	< 0	< 0	15 ± 9	< 0.59	< 0.17
IGR J13490 - 6139	Unclassified	207.26	-61.65	0.24 ± 0.03	< -0.56	< 0.9	2.6 ± 0.9	< 0	< 0	< 1.3	< 0.11
IGR J14059 - 6116	Unclassified	211.49	-61.28	0.16 ± 0.03	< -0.67	< 0.6	< 0	< 0	< 0	< 4.3	< 0.5
4U 1425 - 61	Unclassified	217.25	-61.00	0.19 ± 0.03	< -0.2	< 0.8	< 0	< 0	< 0	< 1.1	< 0.24
2EG J1443 - 6040	Unclassified	220.75	-60.70	0.2 ± 0.04	< -0.2	< 0.3	< 0	< 0	< 0	< 2.3	< 0.6
AX J1510.0 - 5824	Unclassified	227.52	-58.42	0.28 ± 0.05	< 0.17	< 1.0	2 ± 1	< 0	< 0	< 0.7	< 20
IGR J15293 - 5609	Unclassified	232.32	-56.16	0.16 ± 0.03	< -0.27	< 0.4	25 ± 3	2.3 ± 0.7	< 0	< 1.2	< 0.13
MAXI J1535 - 571	Unclassified	233.83	-57.23	0.29 ± 0.03	< -0.55	< 0.8	66 ± 2	12 ± 1	5 ± 3	< 0.19	< 0.019
AGL J1608 - 5253	Unclassified	242.12	-52.88	0.33 ± 0.03	< -0.42	< 0.1	27 ± 1	4.9 ± 0.7	< 0	< 0.7	< 0.48
IGR J18381 - 0924	Unclassified	279.54	-9.41	0.3 ± 0.02	< -0.13	< 0.2	0.2 ± 0.3	< 0	< 0	< 0.7	< 0.24
IRXS J171824.2 - 40293	Unclassified	259.60	-40.49	0.28 ± 0.04	< 0.05	< -0.3	13 ± 2	10 ± 3	< 0	< 0.36	< 0.44
Swift J1713.4 - 4219	Unclassified	258.36	-42.33	0.22 ± 0.03	< -0.2	< -0.3	35 ± 3	23 ± 2	< 0	< 0.13	< 0.022
IGR J18325 - 0756	Unclassified	278.12	-7.95	0.23 ± 0.03	< 0.15	< 0.4	< 0	< 0	< 0	< 0.9	< 0.41
IGR J19094 + 0415	Unclassified	287.42	4.25	0.33 ± 0.03	< 0.1	< 0.8	1.0 ± 0.6	< 0	< 0	< 0.7	< 0.2
IGR J19118 + 1125	Unclassified	287.94	11.42	0.22 ± 0.04	< 0.5	< 0.7	13 ± 3	< 0	16 ± 13	< 1.2	< 0.59
1H 1249 - 637	Unclassified	190.71	-63.06	0.18 ± 0.03	< -0.6	< 0.1	< 0	< 0	< 0	< 2.4	< 1.2
IGR J19239 + 1546	Unclassified	290.98	15.78	0.22 ± 0.02	< -0.4	< 0.8	< 0	< 0	< 0	< 0.9	< 0.24
IGR J19311 + 1708	Unclassified	292.79	17.14	0.16 ± 0.02	< -0.06	< 1.0	< 0	< 0	< 0	< 1.3	< 0.3

Table 13 continued

Table 13 (continued)

Source name	Source type*	R.A.	Dec.	$R_{2-6\text{ keV}}$	$R_{7-40\text{ keV}}$	$R_{25-100\text{ keV}}$	$F_{\text{rms}}1^c$	$F_{\text{rms}}2^d$	$F_{\text{rms}}3^e$	HR1 <sup>a</sup>	HR2 <sup>b</sup>
(1)	(2)	(deg)	(deg)	cts s <sup>-1</sup>	cts s <sup>-1</sup>	cts s <sup>-1</sup>	(8)	(9)	(10)	(11)	(12)
AX J1941.8 + 2251	Unclassified	295.47	22.86	0.15 ± 0.02	< -0.37	< 0.6	< 0	< 0	< 0	< 2.5	< 0.27
1RXS J194211.9 + 25555	Unclassified	295.55	25.93	0.09 ± 0.02	< -0.54	< 0.6	< 0	0.0 ± 0.3	102 ± 57	< 0	< 0.43
AX J1943.5 + 2323	Unclassified	295.89	23.40	0.12 ± 0.02	< -0.52	< 0.2	< 0	< 0	< 0	< 3.1	< 0.49
AX J1946.3 + 2436	Unclassified	296.59	24.61	0.15 ± 0.02	< -0.63	< 0.4	< 0	0.0 ± 0.2	17 ± 162	< 4.9	< 0.36
AX J1949.8 + 2534	Unclassified	297.47	25.57	0.13 ± 0.02	< -0.77	< 0.8	2 ± 1	< 0	3 ± 4	< 2.8	< 0.38
AX J1950.1 + 2628	Unclassified	297.52	26.47	0.11 ± 0.02	< -0.56	< 0.8	< 0	< 0	< 0	< 3.4	< 0.38
4PBC J2008.7 + 3221	Unclassified	302.12	32.35	0.17 ± 0.02	< -0.53	< 0.5	8 ± 1	0.0 ± 0.3	< 0	< 0.55	< 0.27
Swift J195509.6 + 26140	Unclassified	298.79	26.24	0.1 ± 0.02	< -0.59	< 0.5	< 0	< 0	< 0	< 2.2	< 0.26
IGR J20310 + 3835	Unclassified	307.76	38.58	0.2 ± 0.02	< -0.1	< 0.3	5 ± 1	< 0	10 ± 9	< 0.6	< 0.3
gam Cas	Unclassified	14.18	60.72	0.6 ± 0.02	< 0.15	< 1.1	0.06 ± 0.07	< 0	0 ± 1	< 0.57	< 0.09
4U 0033 + 58	Unclassified	9.00	59.00	0.22 ± 0.03	< -0.2	< 0.5	< 0	< 0	< 0	< 3.7	< 0.23
IGR J04539 + 4502	Unclassified	73.56	45.05	0.23 ± 0.03	< -0.5	< 0.5	< 0	< 0	< 0	< 1.2	< 0.18
4U 0854 - 44	Unclassified	133.50	-46.90	0.43 ± 0.04	< -0.4	< 0.8	< 0	< 0	< 0	< 1.1	< 0.23
2CG 284 - 00	Unclassified	155.00	-58.60	0.21 ± 0.03	< -0.29	< 0.2	< 0	0.2 ± 0.5	< 0	< 1.3	< 0.33
MAXI J0911 - 655	Unclassified	137.98	-64.88	0.94 ± 0.07	< 1.5	< 2.7	0.01 ± 0.09	< 0	0.2 ± 1.0	< 1.9	< 0.33
AX J1704.7 - 4109	Unclassified	256.19	-41.16	< 0.33	0.53 ± 0.08	< 0.0	1948 ± 677	14 ± 2	8 ± 2	< 6.8	< 0.42
Swift J1858.6 - 0814	Unclassified	284.67	-8.24	< 0.12	< -0.12	2.1 ± 0.1	< 0	3 ± 1	1.2 ± 0.2	< 1.9	< 0.14
MAXI J1810 - 222	Unclassified	273.12	-22.33	< 0.14	< 0.04	0.9 ± 0.1	1718396 ± 257196	7 ± 3	1.4 ± 0.5	< 0.66	< 0.11
IGR J15479 - 4529	Unclassified	237.06	-45.48	< 0.16	< -0.41	0.7 ± 0.1	12 ± 8	< 0	< 0	< 5.1	< 0.12
IGR J16095 - 3710	Unclassified	242.37	-37.18	< 0.09	< -0.3	0.9 ± 0.2	50907 ± 1678	< 0	< 0	< 10	< 1.2
Oph Cluster	Cluster of Galaxies	258.11	-23.36	2.25 ± 0.03	0.8 ± 0.1	< 1.5	0.34 ± 0.03	1.5 ± 0.6	< 0	0.17 ± 0.02	< 0.039
IGR J17354 - 3255	HMXB Candidate	263.86	-32.93	0.32 ± 0.05	0.37 ± 0.07	< 0.48	127 ± 6	32 ± 4	< 0	< 0.52	< 0.048
IGR J18308 - 1232	Cataclysmic Variable Star	277.71	-12.54	0.27 ± 0.02	< -0.09	< 0.24	< 0	< 0	< 0	< 0.7	< 0.2
AX J1832.3 - 0840	Cataclysmic Variable Star	278.08	-8.68	0.17 ± 0.03	< 0.27	< 0.6	< 0	< 0	< 0	< 1.4	< 0.44
IGR J15539 - 6142	Seyfert 2 Galaxy	238.40	-61.68	0.4 ± 0.05	< -0.2	< 0.9	3 ± 1	< 0	< 0	< 0.7	< 0.16
IGR J11215 - 5952	Blue supergiant star	170.45	-59.86	0.32 ± 0.04	< -0.15	< 0.4	1.7 ± 0.8	8 ± 1	< 0	< 4.7	< 0.11
HR 4492	Variable of RS CVn type	174.87	-65.40	0.19 ± 0.03	< -0.68	< 0.4	< 0	0.1 ± 0.2	< 0	< 1.1	< 0.27
IGR J13186 - 6257	HMXB Candidate	199.60	-62.97	0.35 ± 0.03	< 0.06	< 0.3	0.4 ± 0.3	0 ± 1	< 0	< 1.4	< 0.18
IGR J19443 + 2117	Possible Blazar	295.98	21.31	0.18 ± 0.02	< -0.3	< 1.3	< 0	< 0	< 0	< 3.3	< 0.5
AX J1946.8 + 2512	Emission - line Star	296.71	25.22	0.13 ± 0.02	< -0.65	< 0.5	< 0	< 0	< 0	< 3.5	< 0.38
Cyg A	Seyfert 2 Galaxy	299.87	40.73	0.13 ± 0.02	< -0.4	< 1.1	5 ± 2	< 0	< 0	< 3.4	< 0.32
SS Cyg	Cataclysmic Variable Star	325.68	43.59	0.53 ± 0.03	< 1.8	< 1.8	1.3 ± 0.3	< 0	0 ± 1	0.29 ± 0.04	< 0.09
4U 0022 + 63	SuperNova	6.32	64.16	1.74 ± 0.02	< -0.4	< 0.5	0.02 ± 0.01	< 0	< 0	< 0.52	< 0.054
1ES 0033 + 595	BL Lac - type object	8.97	59.83	0.29 ± 0.02	< -0.1	< 0.4	< 0	2 ± 1	< 0	< 1.4	< 0.17
4U 0446 + 44	Cluster of Galaxies	72.53	45.05	0.76 ± 0.03	< -0.3	< 0.5	< 0	< 0	< 0	< 1.4	< 0.14
4U 0739 - 19	Cluster of Galaxies	116.88	-19.29	0.25 ± 0.03	< -0.2	< 0.4	< 0	< 0	34 ± 70	< 1.9	< 0.21
HD 305560	Blue supergiant star	161.62	-60.56	0.28 ± 0.05	< -0.39	< 0.7	0.5 ± 0.9	< 0	< 0	< 2.5	< 0.25
1H 1045 - 597	Emission - line Star	161.26	-59.69	0.35 ± 0.05	< -0.3	< 0.2	< 0	40 ± 2	< 0	< 0.6	< 0.12

Table 13 continued

Table 13 (continued)

Source name (1)	Source type* (2)	R.A. (deg) (3)	Dec. (deg) (4)	$R_{2-6 \text{ keV}}$ cts s <sup>-1</sup> (5)	$R_{7-40 \text{ keV}}$ cts s <sup>-1</sup> (6)	$R_{25-100 \text{ keV}}$ cts s <sup>-1</sup> (7)	$F_{\text{rms}1^c}$ (8)	$F_{\text{rms}2^d}$ (9)	$F_{\text{rms}3^e}$ (10)	HR1 <sup>a</sup> (11)	HR2 <sup>b</sup> (12)
GX 1 + 4	Symbiotic Star	263.01	-24.75	< 0.16	2.44 ± 0.08	8.9 ± 0.1	103 ± 19	2.0 ± 0.2	0.98 ± 0.04	0.33 ± 0.06	0.15 ± 0.02
IGR J18134 - 1636	Active Galaxy Nucleus	273.37	-16.60	< 0.18	0.87 ± 0.1	< 0.4	< 0	229 ± 7	< 0	< 3.9	< 2.1
GRS 1739 - 278	Cataclysmic Variable Star	265.65	-27.78	< 0.27	1.02 ± 0.1	< 0.2	57 ± 82	6.4 ± 0.9	< 0	< 1.8	< 3.1
SGR 1627 - 41	Gamma - ray Burst	248.97	-47.59	< -0.08	0.74 ± 0.08	< 0.8	< 0	27 ± 1	42 ± 10	< 20	< 10
Circinus Galaxy	Seyfert 2 Galaxy	213.29	-65.34	< 0.19	< 0.1	2.1 ± 0.2	< 0	53 ± 7	0.0 ± 0.1	< 0	< 0.6

NOTE—

<sup>a</sup> and <sup>b</sup> are HR (7–40 keV, 2–6 keV) and HR (25–100 keV, 2–6 keV) calculated with Equation 7, respectively.

**Table 14.** Combined Results of *Insight-HMXT* and MAXI.

Source name	R.A.	Dec	Flux Variability <sup>a</sup>	$\chi^2$	dof	Reduced $\chi^2$
IGR J00291 + 5934	7.26	59.57	stable	26.3	49	0.5
1ES 0033 + 595	8.97	59.83	stable	74.8	104	0.7
GT Mus	174.87	-65.40	stable	72.9	86	0.8
GRO J1008 - 57	152.44	-58.29	variable	69.2	73	0.9
A 0535 + 262	84.73	26.32	variable	69.7	81	0.9
XTE J1829 - 098	277.44	-9.90	variable	102.0	114	0.9
CG 0745 - 1910	116.88	-19.29	stable	62.6	65	1.0
Crab	83.63	22.01	stable	76.9	79	1.0
EXO 2030 + 375	308.06	37.64	variable	124.2	119	1.0
XTE J1908 + 094	287.22	9.38	variable	35.5	36	1.0
SAX J2103.5 + 4545	315.90	45.75	stable	104.5	109	1.0
V407 Cyg	315.54	45.78	stable	91.7	93	1.0
H 1822 - 000	276.34	-0.01	variable	140.2	144	1.0
IGR J17191 - 2821	259.81	-28.30	stable	152.5	150	1.0
SS 433	287.96	4.98	stable	116.1	117	1.0
LSI + 61 303	40.13	61.23	variable	72.8	76	1.0
1E 1841 - 045	280.33	-4.94	variable	109.8	96	1.1
XTE J1901 + 014	285.42	1.44	stable	166.9	148	1.1
GX 304 - 1	195.32	-61.60	stable	98.9	89	1.1
SGR 1833 - 0832	278.44	-8.47	stable	135.2	126	1.1
2S 0921 - 63	140.64	-63.29	stable	39.3	37	1.1
Vela Pulsar and SNR	128.84	-45.18	variable	61.8	57	1.1
4U 1254 - 690	194.40	-69.29	variable	82.5	74	1.1
XTE J1701 - 407	255.43	-40.86	variable	126.2	112	1.1
SS Cyg	325.68	43.59	variable	93.4	82	1.1
Eta Car	161.26	-59.68	stable	80.6	70	1.2
GX 9 + 9	262.93	-16.96	variable	144.4	120	1.2
SAX J1324.5 - 6313	201.16	-63.23	stable	135.0	110	1.2
1E 1145.1 - 6141	176.87	-61.95	stable	93.9	79	1.2
Swift J1845.7 - 0037	281.48	-0.66	stable	180.8	155	1.2
4U 0114 + 65	19.51	65.29	stable	150.8	124	1.2
XTE J1858 + 034	284.68	3.44	stable	155.7	132	1.2
EXO 1722 - 363	261.30	-36.28	variable	186.2	158	1.2
4U 1907 + 09	287.41	9.83	variable	76.6	64	1.2
GS 1843 - 02	282.07	-2.42	variable	90.5	78	1.2

Table 14 continued

**Table 14** (*continued*)

Source name	R.A.	Dec	Flux Variability <sup>a</sup>	$\chi^2$	dof	Reduced $\chi^2$
Gamma Cas	14.18	60.72	stable	139.6	110	1.3
GRS 1716 – 249	259.90	–25.02	variable	153.9	123	1.3
IGR J17379 – 3747	264.50	–37.77	stable	212.9	162	1.3
MAXI J0911 – 655	138.01	–64.87	stable	37.8	30	1.3
Swift J1834.9 – 0846	278.73	–8.73	stable	167.5	133	1.3
GX 301 – 2	186.66	–62.77	variable	142.9	111	1.3
4U 0142 + 61	26.59	61.75	stable	148.9	112	1.3
1H 1556 – 605	240.26	–60.74	variable	78.3	59	1.3
MAXI J1421 – 613	215.41	–61.61	stable	91.5	72	1.3
4U 1850 – 086	283.27	–8.71	variable	229.4	179	1.3
MAXI J1409 – 619	212.01	–61.98	stable	103.0	82	1.3
4U 1210 – 64	183.45	–64.84	variable	129.7	101	1.3
1ES 1959 + 650	300.00	65.15	variable	9.0	7	1.3
2S 1417 – 624	215.30	–62.70	variable	103.8	72	1.4
H 0614 + 091	94.28	9.14	variable	92.7	68	1.4
4U 1957 + 115	299.85	11.71	variable	69.9	49	1.4
4U 1822 – 371	276.45	–37.11	variable	143.7	100	1.4
4U 1543 – 624	236.98	–62.57	variable	107.2	75	1.4
EXO 1846 – 031	282.32	–3.06	variable	176.3	123	1.4
IGR J18410 – 0535	280.25	–5.60	variable	130.9	96	1.4
H 1553 – 542	239.45	–54.41	variable	162.7	119	1.4
1A 1246 – 588	192.42	–59.09	stable	113.3	78	1.5
GRS 1915 + 105	288.80	10.95	variable	121.3	79	1.5
Swift J1728.9 – 3613	262.24	–36.23	variable	262.8	170	1.5
SAX J1828.5 – 1037	277.14	–10.62	variable	178.0	121	1.5
XTE J1946 + 274	296.41	27.37	variable	166.3	113	1.5
RX J1718.4 – 4029	259.60	–40.49	variable	205.4	134	1.5
XTE J1810 – 197	272.46	–19.73	variable	239.3	155	1.5
4U 1626 – 67	248.07	–67.46	variable	20.7	14	1.5
XTE J1739 – 285	264.97	–28.50	variable	140.1	95	1.5
4U 1746 – 37	267.55	–37.05	variable	244.5	150	1.6
Sct X – 1	278.87	–7.62	stable	194.3	121	1.6
Swift J1843.5 – 0343	280.89	–3.72	variable	226.0	136	1.7
XTE J1855 – 026	283.88	–2.61	stable	254.3	150	1.7
4U 1901 + 03	285.90	3.19	variable	250.2	145	1.7
Swift J1822.3 – 1606	275.58	–16.07	variable	329.8	199	1.7
GRS 1747 – 312	267.69	–31.29	variable	216.5	125	1.7

**Table 14** *continued*

**Table 14** (*continued*)

Source name	R.A.	Dec	Flux Variability <sup>a</sup>	$\chi^2$	dof	Reduced $\chi^2$
Tycho SNR	6.32	64.16	stable	239.4	133	1.8
2MASX J16115141 – 6037549	242.96	–60.63	variable	150.8	86	1.8
Ser X – 1	279.99	5.04	variable	243.5	128	1.9
Ophiuchus Cluster	258.11	–23.36	variable	188.5	98	1.9
Terzan 1	263.95	–30.48	variable	306.3	158	1.9
4U 1916 – 053	289.70	–5.24	stable	226.7	122	1.9
XTE J1810 – 189	272.59	–19.07	variable	276.9	147	1.9
H 1743 – 322	266.57	–32.23	variable	280.2	147	1.9
SLX 1746 – 331	267.46	–33.20	variable	332.8	173	1.9
Aql X – 1	287.82	0.58	variable	264.9	132	2.0
4U 1543 – 475	236.79	–47.67	variable	296.9	151	2.0
MAXI J1535 – 571	233.83	–57.23	variable	259.4	127	2.0
MAXI J1735 – 304	263.60	–30.40	variable	263.0	133	2.0
SLX 1735 – 269	264.57	–26.99	variable	193.2	95	2.0
H 1636 – 536	250.23	–53.75	variable	293.5	138	2.1
PSR B1509 – 58	228.48	–59.14	stable	121.5	58	2.1
Pup A	126.03	–43.00	stable	109.3	51	2.1
SAX J1712.6 – 3739	258.14	–37.64	variable	305.8	147	2.1
Cen X – 3	170.32	–60.62	variable	193.9	83	2.3
Swift J1658.2 – 4242	254.55	–42.70	variable	284.7	122	2.3
MAXI J1621 – 501	245.05	–50.04	variable	225.3	93	2.4
OAO 1657 – 41	255.20	–41.66	variable	273.0	111	2.5
GRS 1739 – 278	265.65	–27.78	variable	302.4	122	2.5
IGR J18483 – 0311	282.07	–3.17	variable	232.3	94	2.5
Terzan 2	261.89	–30.80	variable	627.6	216	2.9
4U 1708 – 40	258.10	–40.84	variable	543.2	182	3.0
4U 1624 – 490	247.01	–49.20	variable	309.5	92	3.4
GX 340 + 0	251.45	–45.61	variable	433.3	128	3.4
4U 1538 – 52*	235.60	–52.39	stable	477.5	131	3.6
Vela X – 1	135.53	–40.55	variable	268.2	71	3.8
H 1735 – 444	264.74	–44.45	variable	452.4	117	3.9
NGC 6624	275.92	–30.36	variable	602.7	146	4.1
4U 1323 – 619*	201.65	–62.14	stable	491.7	112	4.4
4U 1954 + 319	298.93	32.10	variable	470.1	108	4.4
GX 349 + 2	256.44	–36.42	variable	938.5	196	4.8
Cyg X – 2	326.17	38.32	variable	131.7	27	4.9
GX 354 – 0	262.99	–33.83	variable	665.3	132	5.0

**Table 14** *continued*



**Table 14** (*continued*)

Source name	R.A.	Dec	Flux Variability <sup>a</sup>	$\chi^2$	dof	Reduced $\chi^2$
Cas A	350.87	58.81	stable	776.3	151	5.1
4U 1755 – 338	269.67	–33.81	variable	888.8	168	5.3
4U 1630 – 472	248.50	–47.39	variable	441.6	80	5.5
GX 339 – 4	255.71	–48.79	variable	914.9	158	5.8
Cyg X – 3	308.11	40.96	variable	506.8	86	5.9
Cir X – 1	230.17	–57.17	variable	922.7	137	6.7
GX 5 – 1	270.28	–25.08	variable	1651.4	241	6.9
1A 1742 – 294	266.52	–29.52	variable	305.8	42	7.3
Galactic Center Region	266.36	–28.98	variable	426.6	50	8.5
GX 3 + 1	266.98	–26.56	variable	976.9	109	9.0
4U 1608 – 52	243.18	–52.42	variable	1365.8	150	9.1
GX 9 + 1	270.38	–20.53	variable	1755.9	188	9.3
4U 1705 – 440	257.23	–44.10	variable	1602.6	144	11.1
H 1730 – 333	263.35	–33.39	variable	905.6	68	13.3
MAXI J1820 + 070	275.09	7.19	variable	889.9	58	15.3
Swift J0243.6 + 6124	40.92	61.43	variable	1780.7	115	15.5
MAXI J1348 – 630	207.05	–63.27	variable	1805.5	114	15.8
GX 13 + 1	273.63	–17.16	variable	2918.8	160	18.2
GS 1826 – 238	277.37	–23.80	variable	3891.8	193	20.2
GX 17 + 2	274.01	–14.04	variable	6787.4	214	31.7
MAXI J1631 – 479	247.80	–47.81	variable	3804.7	92	41.4
Cyg X – 1	299.59	35.20	variable	8552.1	145	59.0

NOTE—

<sup>a</sup> The source is considered as a flux stable one if its  $F_{\text{rms}} - dF_{\text{rms}}$  is less than or equal to  $F_{\text{rms}}$  of Crab at 2–4keV band. Otherwise, the source is marked as ‘variable’ in this table.

\* That many flux variable sources have large reduced  $\chi^2$  is understandable and described in Section 4. However, in addition to Cas A, two flux stable sources (4U 1323–619 and 4U 1538–52) also have large reduced  $\chi^2$ . This is because some data points given by MAXI may be inaccurate. Their long-term light curves monitored by the two missions are shown in Figure 25. As can be seen in panel (b), the long-term light curve of 4U 1538–52 monitored by MAXI has some data points significantly below zero, which is unreasonable. In panel (a), 4U 1323–619 burst in 2019 (between MJD 58500 and 58600) in the long-term light curve monitored by MAXI. *Insight-HXMT* has two observations (MJD 58533.73 and 58533.86) during this period. However, its data indicate that this source was in a quiet state. The corresponding two observational light curves are shown in Figure 26. It can be seen that the results from MAXI are inconsistent with the two observational light curves, and may be influenced by the outbursts of MAXI J1348–630.

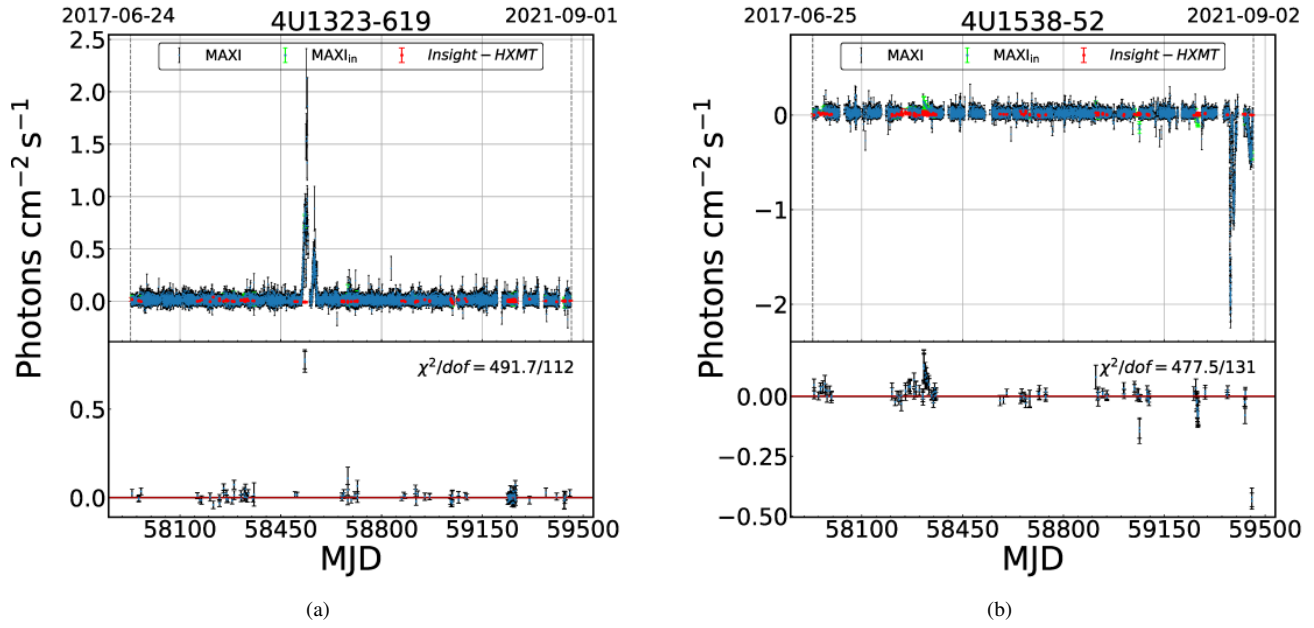


**Figure 25.** The combined results of 4U 1323–619 and 4U 1538–52. The colores and legends are the same as Figure 13.

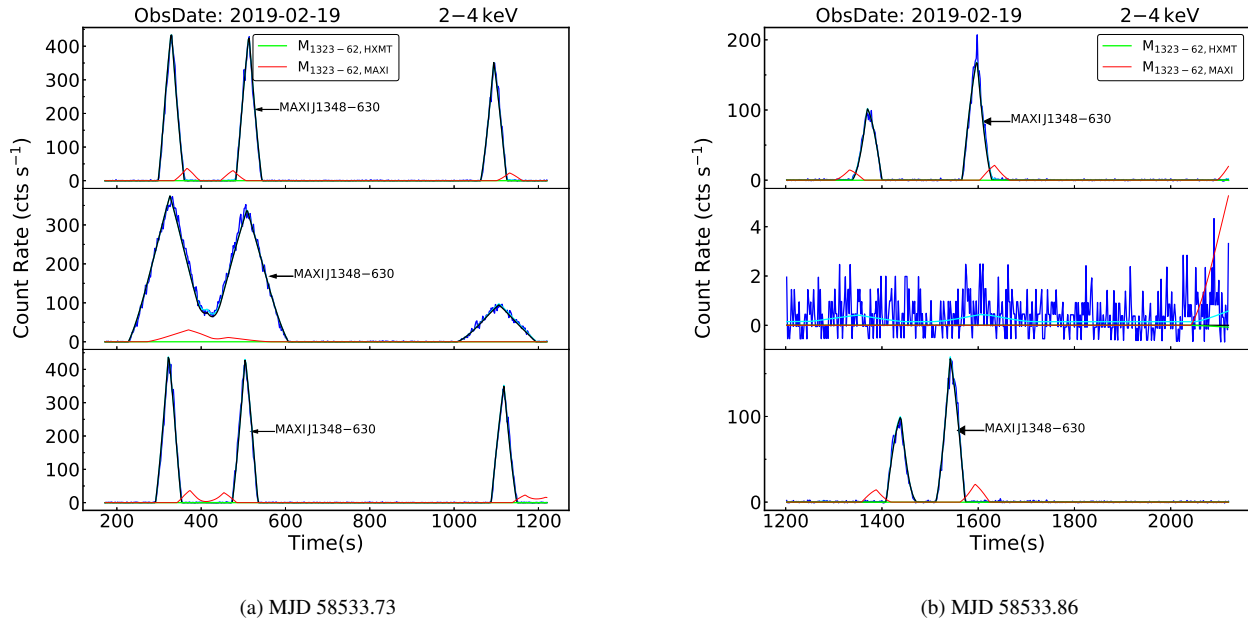


**Figure 26.** Panel (a) shows the light curves crossed 4U 1323–619 observed by *Insight-HXMT* at MJD 58533.73, and comparison between MAXI and *Insight-HXMT*. So does panel (b), while MJD is 58533.86. The blue and cyan lines are light curves and the final fitting results of *Insight-HXMT*. MAXI 1348–630 contributes the most peaks on the light curves, and is colored by black. The green and red lines are the comparison of the contribution by 4U 1323–619 between *Insight-HXMT* and MAXI.